

AD A118767

TR2-82

2

# DEVELOPMENT OF A SYSTEM TO INVERT EDDY-CURRENT DATA AND RECONSTRUCT FLAWS

Harold A. Sabbagh  
L. David Sabbagh  
Analytics, Inc.  
2634 Round Hill Lane  
Bloomington, IN 47401

18 June 1982

FINAL REPORT

Contract No.  
N60921-81-C-0302

Distribution Unlimited:  
Approved for Public Release



DTIC FILE COPY

Prepared for

NAVAL SURFACE WEAPONS CENTER (CODE R34)  
White Oak Labs  
Silver Spring, MD 20910

82 8 27 030

UNCLASSIFIED

SECURITY CLASSIFICATION OF THIS PAGE (When Data Entered)

REPORT DOCUMENTATION PAGE		READ INSTRUCTIONS BEFORE COMPLETING FORM
1. REPORT NUMBER TR2-82	2. GOVT ACCESSION NO. AD-A118767	3. RECIPIENT'S CATALOG NUMBER
4. TITLE (and Subtitle) DEVELOPMENT OF A SYSTEM TO INVERT EDDY-CURRENT DATA AND RECONSTRUCT FLAWS		5. TYPE OF REPORT & PERIOD COVERED FINAL REPORT
7. AUTHOR(s) Harold A. Sabbagh L. David Sabbagh		6. PERFORMING ORG. REPORT NUMBER
9. PERFORMING ORGANIZATION NAME AND ADDRESS Analytics, Inc. 2634 Round Hill Lane Bloomington, IN 47401		8. CONTRACT OR GRANT NUMBER(s) N60921-81-C-0302
11. CONTROLLING OFFICE NAME AND ADDRESS Naval Surface Weapons Center (Code R34) White Oak Labs Silver Spring, MD 20910		10. PROGRAM ELEMENT, PROJECT, TASK AREA & WORK UNIT NUMBERS 62761N, SF61-544, SF61-544-508, 1R348C
14. MONITORING AGENCY NAME & ADDRESS (if different from Controlling Office)		12. REPORT DATE 18 June 1982
		13. NUMBER OF PAGES 46
		15. SECURITY CLASS. (of this report) Unclassified
		15a. DECLASSIFICATION/DOWNGRADING SCHEDULE
16. DISTRIBUTION STATEMENT (of this Report)  Distribution Unlimited: Approved for Public Release		
17. DISTRIBUTION STATEMENT (of the abstract entered in Block 20, if different from Report)		
18. SUPPLEMENTARY NOTES		
19. KEY WORDS (Continue on reverse side if necessary and identify by block number) Eddy-currents                      Linear and nonlinear least-squares Nondestructive evaluation       LINPACK/MINPACK Numerical inversion              Integral equations Flaw reconstruction              Method of moments		
20. ABSTRACT (Continue on reverse side if necessary and identify by block number) Starting from rigorous electromagnetic theory, a model for the inversion of eddy-current data to reconstruct flaws in circular cylindrical tubes is developed. The form of the model consists of integral equations, whose kernels (Green's functions) are computed using Fourier transforms. The unknowns in the principal integral equation are the conductivity and electric field in the flawed region. Because these unknowns appear multiplied together, the problem is really nonlinear. The integral → cont		

DD FORM 1 JAN 73 1473

EDITION OF 1 NOV 65 IS OBSOLETE  
S/N 0102-LF-014-6601

UNCLASSIFIED

SECURITY CLASSIFICATION OF THIS PAGE (When Data Entered)

UNCLASSIFIED

SECURITY CLASSIFICATION OF THIS PAGE (When Data Entered)

*cont*  
equations are converted to algebraic (vector-matrix) form by means of the method of moments. The inversion process is completed by applying linear and nonlinear least-squares algorithms, that are contained in the commercially available LINPACK/MINPACK software packages, to these algebraic equations. Using these algorithms in the model, we have reconstructed numerically-generated flaws with great accuracy, both when the flaws are "deterministic" and "random", the latter with data that has been perturbed by as much as 20%. Examples of these inversions, using both the linear and nonlinear algorithms, are presented. In addition, the model can be extended in a straightforward way to include the effects of known irregularities, such as tube supports or tube-flaring, on the reconstruction of flaws.

Accession For	
THIS GRIAT	<input checked="checked" type="checkbox"/>
INFO TAB	<input type="checkbox"/>
Unannounced	<input type="checkbox"/>
Justification	
By _____	
Distribution/ _____	
Availability Codes	
Avail and/or	
Dist Special	
A	



UNCLASSIFIED

SECURITY CLASSIFICATION OF THIS PAGE (When Data Entered)

## I. INTRODUCTION

Eddy-current testing was first systematically studied in Germany during World War II, but did not receive wide recognition until Forster and his colleagues published the results of their extensive theoretical, experimental and industrial investigations between 1952 and 1954 [1]. These papers did not include a quantitative theory for flaw detection, however, and it was not until 1964 that Burrows constructed such a theory in his dissertation [2]. His idea, which was based on electromagnetic theory, is to replace the flaw by an equivalent dipole, and is reasonable if the flaw is small compared with the skin depth (sometimes called the diffusion length) of the eddy-currents.

The work of Dodd, et al. [3-5] brought eddy-current nondestructive evaluation (NDE) "of age" by showing how one could get useful analytical results based on a rigorous application of electromagnetic theory. Their theory of flaw detection contains Burrows' and is subject to the same limitations of dipole representation. Equally significant with their use of rigorous electromagnetic theory, in our opinion, is their development of computer programs to compute the integral representations of the electromagnetic fields [6-7]. Now the modern era of eddy-current inspection is upon us, based on the union of numerical methods in mathematics and rigorous electromagnetic theory.

As further evidence of this, we cite the extensive research supported by the Electric Power Research Institute (EPRI) [8], in particular the work of W. Lord, of Colorado State University, B. A. Auld, of Stanford University, and A. N. Mucciardi, of Adaptronics, Inc. Lord is developing a finite element model for eddy-current nondestructive testing phenomena, whereas Auld is using the reciprocity theorem of electromagnetics to quantitatively model flaw responses in eddy-current testing. Finally, Mucciardi is developing a system for flaw detection and classification by using an adaptive learning network for eddy-current signal analysis.

In this report we describe an approach to the reconstruction of flaws, not merely their detection. This will give us the ability to

obtain much more information about the nature of the flaw, unimpeded by the size restriction of the dipolar approximation that was mentioned above. By "flaw" we mean virtually any departure of the medium from a standard condition, which is known a priori, such as may be produced not only by a crack but also by conductivity inhomogeneities produced by stresses, magnetite build-up, etc. Our approach is very much in the spirit of contemporary work in inverse methods in electromagnetics [9-11] and electromagnetic-geophysical prospecting [12-19].

At this point we introduce some systems-related ideas that should make clearer the way our concept of inversion is to be used for non-destructive evaluation. Refer to Figure 1, which shows a "system," together with its input and output. In part (a) of the figure the input is known and so is the system, and the output is to be determined. This is the "forward" or "direct" problem. For example, the input could be a current or voltage source, and the system, a coil coupled to the workpiece. The output, the magnetic vector potential or induced eddy-current within the workpiece, can be directly computed in a straightforward manner by electromagnetic theory.

In part (b) the system and output are known, and the input is to be determined. This is a problem of communication theory, or signal detection. One assumes a catalog of possible input signals to be available, whose structure and characteristics are known a priori; from the known output one estimates the input signal on the basis of the maximum a posteriori probability of its occurrence. This is the basis of Adatronics' flaw detection system. Their input data base (the catalog of possible input signals) consists of 506 defect waveforms under tube supports and 261 isolated defect waveforms, all of which are at 400 kHz.

This is an example of another "forward" method, and appears to be sufficient for many applications. It is, however, limited by both the large volume of signal waveforms that must be catalogued for a suitable generalized interpretation and by the subjective comparisons made by the interpreter. The method also gives little indication of the sensitivity of the solution to possible errors in the data and the degree of non-uniqueness associated with the chosen mode.

In Figure 1(c) both the input and output are known and the system is unknown. The input could be a known "probing" signal, and the output, the measured response to the probe. The object is to determine the nature of the system. This is an example of "system identification" or "parameter estimation," where "parameter" refers to certain parameters of the unknown system. In the sense that problems (a) and (b) are "direct," problem (c) is the "indirect" or "inverse" problem, and is the problem discussed in this report. What one seeks in this problem is a model-system that, when operating on the input, produces a "model-output" that is, in some sense, an optimum estimation of the known output.

There are two common ways of obtaining a sufficient amount of independent data to estimate parameters in eddy-current testing: (a) through the use of multiple coils, and (b) through the use of multiple frequencies, including pulses or transient signals [20]. Of course a combination of the two may be used. In this report we consider only the multiple coil method.

In Figure 2 we show a system of coaxial coils within a tube that is to be inspected. Within the wall of the tube is located an anomalous region (the "flaw") that we wish to reconstruct. A mathematical mesh is defined that surrounds the anomaly, as shown. The properties of the mesh, such as its location, size, and fineness, are known to us. What we don't know are the values of the electrical conductivity to assign to each rectangle of the mesh. The "system," then, consists of the coils, the tube, and the mesh that encloses the anomalous region. The unknown parameters that are to be estimated in order that the system be "identified," in the sense of Figure 1(c) and its discussion, are the conductivities that are to be assigned to each rectangle of the mesh. The known input is the current to the exciting coil, and the known outputs are the voltages induced into the sensing coils. Clearly, if we can determine the conductivity map that is defined on the mesh, we will have reconstructed the anomalous region.

The method of solving this problem is based on minimizing the square of the error between the actual measured data and that produced by the model-system, the model-output (this error is often called the

residual). The parameters that are varied to produce the optimum model, in the least-squares sense, are, of course, the conductivities that are assigned to each cell in the mesh of Figure 2.

Thus, mathematically, we wish to determine a set of unknown parameters  $\sigma_j$ ,  $j=1, \dots, M$ , where  $M$  is the number of cells in the mesh, from a set of data,  $e_i$ ,  $i=1, \dots, N$ , where  $e_i$  are the voltages induced into the  $N$  sensing coils. The  $e_i$  are functionally related to the  $\sigma_j$  in a known way; that is

$$e_1 = f_1(\sigma_1, \dots, \sigma_M) \quad (1)$$

$$e_2 = f_2(\sigma_1, \dots, \sigma_M)$$

.

.

.

$$e_N = f_N(\sigma_1, \dots, \sigma_M)$$

Hence, given the  $\sigma_j$  we can calculate the  $e_i$  by treating this as a "forward" problem, in the sense of Figure 1(a). The equations (1) that define the forward problem are determined by using electromagnetic theory.

But it is the voltages,  $e_i$ , that are the given data, so we must invert the system, (1), to determine the  $\sigma_j$ . We do this by minimizing the error function

$$F(\sigma_1, \dots, \sigma_M) = \left[ \sum_{i=1}^N (e_i - f_i)^2 \right]^{1/2} \quad (2)$$

Iterative methods are commonly used to carry out the minimization of (2). The iterative method successively improves a current model, i.e., a current estimate of the  $\sigma_i$ , until the error measure, (2), is small and the parameters are stable with respect to reasonable changes in the model.

The success of this method of inversion depends largely on the availability of suitable numerical algorithms for carrying out the

least-squares solution of (1). Any algorithm chosen must contend with the fact that the problem as posed in (1) and (2) is generally quite ill-conditioned, which means that small variations in input data can produce quite large variations in the solution. The commercially available FORTRAN packages, LINPACK [21] and MINPACK [22], contain well-written codes for least-squares algorithms, and these codes served as the basis of the numerical experiments to be described in this report. LINPACK consists of linear equation-solving algorithms, and MINPACK contains nonlinear least-squares algorithms. A description of these algorithms will be given in a later section of this report.

These experiments indicate that the inversion method works quite well on simulated flaws, even when the data is corrupted by as much as 20%; this is quite important in applications. Another nice feature is that once the nonlinear inversion algorithm has converged, it is possible, using the techniques of linear inverse theory, to assess the errors and resolution in the estimate of the final model. The objective is to determine which features of the model are well-resolved and important to the interpretation of the data and which features are irrelevant, in the sense that the data neither support nor reject their inclusion in the model. This is also quite useful in eddy-current NDE.

## II. DERIVATION OF THE MODEL SYSTEM

### (a) Integral Equations

The detection of flaws, or anomalies, by means of eddy-currents depends upon the fact that flaws are not electrically conducting and that the eddy-current flow is interrupted at the boundary of the flaw. The flaw, therefore, can be considered to be an inhomogeneity, which consists of a conductivity,  $\sigma_f$ , that is imbedded in a region whose conductivity,  $\sigma_0$ , is known a priori. The dielectric constant and magnetic permeability of each region are those of free space,  $\epsilon_0$  and  $\mu_0$ . Hence, Maxwell's equations for the two regions are:

$$\nabla \times \bar{E}_0 = -j\omega\mu_0 \bar{H}_0 \quad (\text{Known Region}) \quad (3)(a)$$

$$\nabla \times \bar{H}_0 = (\sigma_0 + j\omega\epsilon_0) \bar{E}_0$$

$$\nabla \times \bar{E}_f = -j\omega\mu_0 \bar{H}_f \quad (\text{Flawed Region}) \quad (3)(b)$$

$$\nabla \times \bar{H}_f = (\sigma_f + j\omega\epsilon_0) \bar{E}_f$$

Upon subtracting (3)(b) from (3)(a), we get

$$\nabla \times (\bar{E}_0 - \bar{E}_f) = -j\omega\mu_0 (\bar{H}_0 - \bar{H}_f)$$

$$\nabla \times (\bar{H}_0 - \bar{H}_f) = \sigma_0 (\bar{E}_0 - \bar{E}_f) + j\omega\epsilon_0 (\bar{E}_0 - \bar{E}_f) + (\sigma_0 - \sigma_f) \bar{E}_f. \quad (4)$$

Now we have added and subtracted  $\sigma_0 \bar{E}_f$  to get the final form.

Thus, the perturbation of the electromagnetic field,  $\bar{E}_0 - \bar{E}_f$ ,  $\bar{H}_0 - \bar{H}_f$ , satisfies the same equation as the original electromagnetic field within the known region, except for the presence of the term  $(\sigma_0 - \sigma_f) \bar{E}_f$ . This term, which is equivalent to a current source,  $\bar{J}_a$ , represents the presence of the anomalous region, or flaw. It is important to note that  $\bar{J}_a$  vanishes off of the flaw, because there  $\sigma_f = \sigma_0$ .

In the usual way we can derive a vector wave equation for  $\bar{E}_0 - \bar{E}_f$  from (4):

$$\begin{aligned} \nabla \times \nabla \times (\bar{E}_0 - \bar{E}_f) &= -j\omega\mu_0 \nabla \times (\bar{H}_0 - \bar{H}_f) \\ &= (\omega^2 \mu_0 \epsilon_0 - j\omega\mu_0 \sigma_0) (\bar{E}_0 - \bar{E}_f) - j\omega\mu_0 (\sigma_0 - \sigma_f) \bar{E}_f. \end{aligned} \quad (5)$$

By treating the last term in (5) as a source, we can immediately write down a formal solution for the perturbed field  $\bar{E}_0 - \bar{E}_f$ :

$$(\bar{E}_0 - \bar{E}_f)(\bar{r}) = j\omega\mu_0 \iiint_{\text{Flaw}} \bar{G}(\bar{r}|\bar{r}') \cdot \bar{E}_f(\bar{r}') (\sigma_0 - \sigma_f)(\bar{r}') d\bar{r}' \quad (6)$$

where  $\bar{G}(\bar{r}|\bar{r}')$  is the dyadic Green's function for the known region [23], and the volume of integration is the flawed region, for which  $\sigma_0 - \sigma_f \neq 0$ . This equation is the basis for our inversion technique. Before going further with it, we make the following observations which will allow us to reduce the problem to a scalar system.

In eddy-current NDE work, we don't measure perturbed fields directly; rather, the perturbed EMF that is induced in a probe coil is measured. Such an EMF is given by the line integral of (6) along the probe coil windings. In the system that we are investigating, as shown in Figure 2, the EMF is the line integral of the azimuthal electric field,  $E_\phi$  (in the usual cylindrical coordinate system, wherein the z-axis coincides with the axis of the tube). Hence, all we need to consider is that single component of the  $\bar{E}$  vector. In addition, we can ignore any  $\phi$ -variations of  $E_\phi$ , because the line integral is taken over  $2\pi$  radians/turn of the probe coil. Therefore, if we expand  $E_\phi$  in a Fourier series,  $\{\cos n\phi\}$ , then only the  $n=0$  term will contribute a non-zero value to the EMF integral. But if  $E_\phi$  is independent of  $\phi$ , then the  $\bar{E}$  vector field (which, by assumption, consists of only the  $\phi$ -component) is divergenceless. This is equivalent to saying that the Green's function of (6) is the electric field that is produced by a circular filament of current, of radius  $r'$ , located at the plane  $z=z'$ . In addition, we can also take the "anomalous current,"  $\bar{J}_a$ , to be wholly in the  $\phi$ -direction, and divergenceless.

Thus, we can reduce (6) to the scalar equation

$$(E_0 - E_f)(r, z) = -j\omega\mu_0 \iint_{\text{Flaw}} G(r, z; r', z') E_f(r', z') (\sigma_0 - \sigma_f)(r', z') r' dr' dz' , \quad (7)$$

where  $E_0$ ,  $E_f$ , and  $G$  are the  $\phi$ -components of their respective fields. The gist of the preceding argument is that, by using coils, as shown in Figure 2, we are unable to determine the azimuthal location or extent of the flaw. In carrying out the integral over  $\phi$  in (6), thereby transforming

it into the two-dimensional integral, (7), we assume that the flaw is confined to the plane  $\phi=0$ . This means that the flaw has the functional dependence

$$(\sigma_0 - \sigma_f)(r, z, \phi) = \delta(\phi)(\sigma_0 - \sigma_f)(r, z) \quad .$$

In order to further develop the model, we must take into account that the region of interest consists of three parts: the interior of the tube, the tube wall, and the region exterior to the tube. We call these regions 1, 2, 3, respectively, and introduce the following notation for the Green's function:

$$\begin{aligned} G_{ij}(r, z; r', z') &= \text{Field produced at } (r, z) \text{ in region } i, \\ &\quad \text{due to filamentary current loop at } (r', z') \\ &\quad \text{in region } j \\ &= G_{ji}(r', z'; r, z), \quad i, j = 1, 2, 3 \quad . \end{aligned}$$

The last equation, a reciprocity relation, follows because the magnetic permeability of all three regions is the same (this, and other matters relating to Green's functions in stratified media, can be found in [23]).

We introduce the following notation

$$E_{1,2}(r, z) = \text{Electric field in region 1 or 2, with flaw present}$$

$$E_0(r, z) = \text{Electric field with flaw absent, due to exciting coil.}$$

Then (7) produces the following basic integral equation for computing  $E$  in the flawed region, which is in region 2:

$$\begin{aligned} E_2(r, z) + j\omega\mu_0\sigma_0 \iint_{\text{Flaw}} G_{22}(r, z; r', z') E_2(r', z') \left( \frac{\sigma_f(r', z')}{\sigma_0} - 1 \right) r' dr' dz' \\ = E_0(r, z) \end{aligned} \quad (8)$$

In addition, we have the integral relation for computing the perturbed electric field at the probe coil (which lies within region 1):

$$(E_0 - E_1)(r, z) = j\omega\mu_0\sigma_0 \iint_{\text{Flaw}} G_{12}(r, z; r', z') E_2(r', z') \cdot \left( \frac{\sigma_f}{\sigma_0}(r', z') - 1 \right) r' dr' dz' \quad (9)$$

When this equation is integrated over the probe coil we get the perturbed EMF. If we assume that the probe coil is uniformly and densely wound with  $n_c$  turns per unit area (in the  $r$ - $z$  plane), we get for this EMF:

$$\text{EMF} = -2\pi n_c \iint_{\text{Probe Coil}} (E_0 - E_1) r dr dz \quad (10)$$

Finally, the electric field,  $E_0$ , that is produced by the exciting coil is given by

$$\begin{aligned} E_0(r, z) &= -j\omega\mu_0 2\pi \iint_{\substack{\text{Exciting} \\ \text{Coil}}} G_{21}(r, z; r', z') J_0(r', z') r' dr' dz' \\ &= -j\omega\mu_0 2\pi n_e I_0 \iint_{\substack{\text{Exciting} \\ \text{Coil}}} G_{21}(r, z; r', z') r' dr' dz' \quad (11) \end{aligned}$$

where  $J_0$  is the exciting coil current density,  $n_e$  is the density of turns in the exciting coil, and  $I_0$  is the current carried by the exciting coil.

Equations (8)-(11) constitute the model system. The algorithm for using the system consists of first computing the incident field,  $E_0$ , at the flaw, by (11); this is the right-hand side of (8). For a given distribution of flaw conductivity,  $\sigma_f(r, z)$ , (8) can be solved numerically. Its solution, the electric field,  $E_2$ , in the flawed region is the source term for (9), which produces the perturbed electric field at the probe

coil in region 1. The integral of the perturbed electric field produces the perturbed EMF, (10), which is then compared with the measured EMF to determine if the assumed flaw conductivity,  $\sigma_f(r,z)$ , is "close" to the actual (though unknown) flaw conductivity. The problem is really non-linear because (8) involves the product of two unknowns,  $\sigma_f(r,z)$  and  $E_2(r,z)$ . Thus, some form of iteration is required, in which one starts with an assumed distribution for  $\sigma_f(r,z)$ , and then hopes to converge to a final acceptable value.

The model that we have developed is quite general. Crucial its application as a reconstruction technique is the ability to compute the Green's function of the "known" region, i.e., the region that exists in the absence of any flaws. When the known region consists of a cylindrical tube, then the Green's function can be computed in a straightforward manner by the use of Fourier transforms and algebra; we carry out these computations in Appendix A.

If, however, we wish to reconstruct flaws that exist in the presence of tube supports, as in Figure 3, or tube flaring, as in Figure 4, or any other known irregularities, then we cannot hope to compute the Green's function in a purely analytical manner. In this case the Green's function satisfies an integral equation, which must be solved numerically. We hardly consider this to be a very serious drawback, however, because so much of our modeling effort involves the numerical solution of integral equations.

The integral equation that is satisfied by the Green's function is identical to (8), with the following changes:  $G_{22}$  is the Green's function of the cylindrical tube, as if there were no irregularities (the subscripts may be different, depending upon the location and type of known irregularity),  $\sigma_f(r',z')$  becomes the conductivity of the known irregularity, and the integration is over the volume occupied by the irregularity, and the right-hand side is replaced by  $G_{22}$ . Of course, we are still interested in only the  $\phi$ -component of the Green's function, and that is why we can use the scalar integral equation, (8). If, in (8), there is no irregularity, then  $\sigma_f = \sigma_0$ , and the Green's function is identical to that for the circular cylinder.

An additional complication exists when the region is more irregular than a cylinder, and that is the need to approximate the region in order to apply the method of moments (or any other numerical method). In Figure 5 we show two methods of approximating a curved surface with splines of zero-order and first-order. Higher-order approximating functions could also be used, but the two shown in Figure 5 are the easiest to work with.

(b) Discretization of the Model: The Method of Moments [24]

The discretization of the problem via the method of moments is based on the use of a mesh, as shown in Figure 2. In order to reduce (8) to an algebraic system, we expand  $E_2(r, z)$  and  $(\sigma_f/\sigma_0 - 1)$  in pulse functions that are defined with respect to this mesh:

$$E_2(r, z) = \sum_{j=1}^{N_c} E_j P_j(r, z) \quad (12)(a)$$

$$\left(\frac{\sigma_f}{\sigma_0}(r, z) - 1\right) = \sum_{j=1}^{N_c} \sigma_j P_j(r, z) \quad , \quad (b)$$

where  $N_c$  is equal to the number of cells in the mesh, and  $P_j(r, z)$  is the  $j$ th pulse function, which is defined by

$$\begin{aligned} P_j(r, z) &= 1 \quad , \quad (r, z) \text{ in } j\text{th cell} \\ &= 0 \quad , \quad \text{otherwise} \quad . \end{aligned} \quad (13)$$

The  $j$ th expansion coefficients,  $E_j$ ,  $\sigma_j$ , are the constant values of the fields over the  $j$ th cell.

Because  $E_2$  and  $(\sigma_f/\sigma_0 - 1)$  have identical expansions in non-overlapping pulse functions, it follows that their product does also:

$$E_2(r, z)(\sigma_f(r, z)/\sigma_0 - 1) = \sum_{j=1}^{N_c} E_j \sigma_j P_j(r, z) \quad . \quad (14)$$

Upon substituting (12) and (14) into (8), we get

$$\sum_{j=1}^{N_c} E_j P_j(r, z) + j\omega\mu_0\sigma_0 \sum_{j=1}^{N_c} E_j \sigma_j \iint_{\text{Flaw}} G_{22}(r, z; r', z') P_j(r', z') r' dr' dz' = E_0(r, z) \quad (15)$$

Next, we take moments of (15); i.e., we multiply (15) by weighting functions,  $Q_i(r, z)$ ,  $i = 1, \dots, N_c$ , and integrate over the flaw. If the weighting functions are delta functions that are located at the center of each cell, then the method is called point-matching; if they are the same functions that were used in the expansions, (12), then the method is called Galerkin's method. In any case, the result is the system of  $N_c$  equations:

$$\begin{aligned} & \sum_{j=1}^{N_c} E_j \iint_{\text{Flaw}} P_j(r, z) Q_i(r, z) r dr dz \\ & + \sum_{j=1}^{N_c} E_j \sigma_j j\omega\mu_0\sigma_0 \iint_{\text{Flaw}} r dr dz \iint_{\text{Flaw}} G_{22}(r, z; r', z') P_j(r', z') Q_i(r, z) r' dr' dz' \\ & = \iint_{\text{Flaw}} E_0(r, z) Q_i(r, z) r dr dz, \quad i = 1, \dots, N_c \end{aligned} \quad (16)$$

The vector-matrix version of (16) is:

$$(\bar{A} + j\omega\mu_0\sigma_0\bar{G})\bar{E} = \bar{F}, \quad (17)$$

where

$$A_{ij} = \iint_{\text{Flaw}} Q_i(r, z) P_j(r, z) r dr dz \quad (18)(a)$$

$$G_{ij} = \sigma_j \iint_{\text{Flaw}} Q_i(r, z) r dr dz \iint_{\text{Flaw}} G_{22}(r, z; r', z') P_j(r', z') r' dr' dz' \quad (b)$$

$$F_i = \iint_{\text{Flaw}} E_0(r, z) Q_i(r, z) r dr dz, \quad i, j = 1, \dots, N_c \quad (c)$$

Our analysis has been based on the method of point-matching, with  $Q_i(r, z) = \delta(r - r_i) \delta(z - z_i) / r$ , where  $(r_i, z_i)$  are the coordinates of the midpoint of the  $i$ th cell. Point-matching generally takes better advantage of the singularity in the Green's function to produce a better conditioned matrix (i.e., one more diagonally dominant) for inversion. The disadvantage of point-matching is that the infinite integrals that define the various matrix elements in  $G_{ij}$  and  $F_i$  (see Appendix B) do not converge as rapidly as with Galerkin's method, so one has to take more care in their numerical evaluation. This has not turned out to be a problem, however.

Thus, upon letting  $(z_j^-, z_j^+)$  be the lower and upper  $z$ -limits, respectively, and  $(r_j^-, r_j^+)$  the lower and upper  $r$ -limits, respectively, of the  $j$ th cell, we get

$$A_{ij} = \int_{r_j^-}^{r_j^+} \int_{z_j^-}^{z_j^+} \frac{\delta(r - r_i) \delta(z - z_i)}{r} r dr dz = \delta_{ij} \quad (19)(a)$$

$$G_{ij} = \sigma_j \int_{r_j^-}^{r_j^+} \int_{z_j^-}^{z_j^+} G_{22}(r_i, z_i; r', z') r' dr' dz' \quad (b)$$

$$F_i = E_0(r_i, z_i) = -j\omega\mu_0 2\pi n_e I_0 \iint_{\substack{\text{Exciting} \\ \text{Coil}}} G_{21}(r_i, z_i; r', z') r' dr' dz' \quad (c)$$

where  $\delta_{ij} = 1$ , if  $i = j$ , and  $= 0$ , if  $i \neq j$ . Similarly, when (14) is substituted into (9), we get:

$$(E_0 - E_1)(r, z) = j\omega\mu_0\sigma_0 \sum_{j=1}^{N_c} \sigma_j E_j \int_{r_j^-}^{r_j^+} \int_{z_j^-}^{z_j^+} G_{12}(r, z; r', z') r' dr' dz' \quad (20)$$

Now we define the  $k$ th probe coil as one having an inner radius,  $\rho_1$ , outer radius,  $\rho_2$ , left-hand  $z$ -coordinate,  $\zeta_k^-$ , right-hand  $z$ -coordinate,  $\zeta_k^+$ , and midpoint  $z$ -coordinate of  $\zeta_k$ . Then the EMF induced into the  $k$ th probe coil is given by substituting (20) into (10):

$$\text{EMF}(k) = -j\omega\mu_0\sigma_0 2\pi n_c \sum_{j=1}^{N_c} \sigma_j E_j \int_{\rho_1}^{\rho_2} r dr \int_{\zeta_k^-}^{\zeta_k^+} dz \int_{r_j^-}^{r_j^+} \int_{z_j^-}^{z_j^+} G_{12}(r, z; r', z') r' dr' dz' \quad (21)$$

$k = 1, \dots, K$

This, too, can be put into vector-matrix form:

$$\vec{\text{EMF}} = \vec{T}(\vec{\sigma E}), \quad (22)$$

where

$$T_{kj} = -j\omega\mu_0\sigma_0 2\pi n_c \int_{\rho_1}^{\rho_2} r dr \int_{\zeta_k^-}^{\zeta_k^+} dz \int_{r_j^-}^{r_j^+} \int_{z_j^-}^{z_j^+} G_{12}(r, z; r', z') r' dr' dz' \quad (23)$$

is the transfer function from the  $j$ th cell to the  $k$ th coil. Note that the number of coils,  $K$ , is not necessarily equal to the number of cells,  $N_c$ . Indeed, in applying the method of least-squares to this model, we take  $K = 50$ , which produces 100 real and imaginary components of EMF, and  $N_c = 60$ . This yields an overdetermined system, which is typical of least-squares problems.

In Appendix B we derive expressions for the various vector-matrix elements that have just been defined.

### III. LEAST-SQUARES ALGORITHMS: LINPACK AND MINPACK

Now that we have a model system in hand, we shall say more about the mathematical and numerical solutions of linear and nonlinear least-squares problems. We rewrite (1) as the vector equation

$$\bar{e} = \bar{f}(\bar{\sigma}) \quad (24)$$

We seek a least-squares solution, as defined below. Let

$$\bar{F}(\bar{\sigma}) = \bar{f}(\bar{\sigma}) - \bar{e} \quad (25)$$

Upon introducing the usual squared-norm notation, we have

$$||\bar{F}(\bar{\sigma})||_2 = ||\bar{f}(\bar{\sigma}) - \bar{e}||_2 = \left[ \sum_{i=1}^N [f_i(\sigma_1, \dots, \sigma_M) - e_i]^2 \right]^{1/2} \quad (26)$$

Then the definition of a least-squares solution of (24) is: given  $\bar{e} = (e_1, \dots, e_N)$ , find  $\sigma = (\sigma_1, \dots, \sigma_M)$  that minimizes  $||F||_2$ ; i.e., solve

$$\min_{\bar{\sigma}} ||\bar{f}(\bar{\sigma}) - \bar{e}||_2 \quad (27)$$

We first consider the case where  $\bar{f}$  is linear. Then write (24), (25), and (27), respectively, as

$$\bar{e} = \bar{A} \bar{\sigma} \quad (28)$$

$$\bar{r} = \bar{e} - \bar{A} \bar{\sigma} \quad (29)$$

$$\min_{\bar{\sigma}} ||\bar{e} - \bar{A} \bar{\sigma}||_2 \quad (30)$$

If  $\bar{\sigma}^*$  is a solution of (30), then it is known that [25]

$$\bar{A}^T \bar{r}^* = \bar{A}^T (\bar{e} - \bar{A} \bar{\sigma}^*) = 0 \quad (31)$$

where the superscript, T, denotes the transpose of a matrix. Thus

$$\bar{A}^T \bar{A} \sigma^* = \bar{A}^T e \quad (32)$$

or

$$\sigma^* = \bar{A}^+ e, \quad (33)$$

where  $\bar{A}^+ = (\bar{A}^T \bar{A})^{-1} \bar{A}^T$  is the pseudoinverse of  $\bar{A}$ . While (33) characterizes the mathematical solution of (30), we don't actually numerically compute  $\bar{A}^+$ ; for numerical solutions other methods are used.

A standard method of solving (30) is to use the QR-factorization of the matrix  $\bar{A}$ . Given that  $\bar{A}$  is  $N \times M$  (where  $N \geq M$ ), there exists an orthogonal matrix  $\bar{Q}$  (of order  $N \times N$ ) such that

$$\bar{Q}^T \bar{A} = \begin{bmatrix} \bar{R} \\ \bar{O} \end{bmatrix}, \quad (34)$$

where  $\bar{R}$  is upper triangular. If we write  $\bar{Q} = [\bar{Q}_1, \bar{Q}_2]$ , where  $\bar{Q}_1$  has  $M$  columns, then

$$\bar{A} = \bar{Q}_1 \bar{R} \quad (35)$$

Thus if  $\text{rank}(\bar{A}) = M$ , the columns of  $\bar{Q}_1$  form an orthonormal basis for the column space of  $\bar{A}$ . Now if  $\bar{A} = [\bar{A}_1, \bar{A}_2]$ , where  $\bar{A}_1$  has  $k$  columns,

and if  $\bar{R} = \begin{bmatrix} \bar{R}_{11} & \bar{R}_{12} \\ \bar{O} & \bar{R}_{22} \end{bmatrix}$  where  $\bar{R}_{11}$  is  $k \times k$ , then

$$\bar{Q}^T \bar{A}_1 = \begin{bmatrix} \bar{R}_{11} \\ \bar{O} \end{bmatrix}. \quad (36)$$

Hence  $\bar{Q}$  and  $\bar{R}_{11}$  give a QR-factorization of  $\bar{A}_1$ . This truncated decomposition is important for matrices whose rank is less than full, i.e., for which  $\text{rank}(\bar{A}) < \min(M, N)$ .

This orthogonal triangularization is generated by Householder transformations [21, 25]. Once we have this triangularization, then the solution to (30) follows:

$$\bar{Q}^T \bar{r} = \bar{Q}^T \bar{e} - \bar{Q}^T \bar{A} \bar{\sigma} \quad (37)$$

$$\bar{Q}^T \bar{r} = \begin{bmatrix} \bar{e}_1 \\ \bar{e}_2 \end{bmatrix} - \begin{bmatrix} \bar{R} \\ \bar{0} \end{bmatrix} \sigma, \quad \text{where} \quad \begin{bmatrix} \bar{e}_1 \\ \bar{e}_2 \end{bmatrix} = \bar{Q}^T \bar{e} \quad (38)$$

$$\bar{Q}^T \bar{r} = \begin{bmatrix} \bar{e}_1 - \bar{R}\sigma \\ \bar{e}_2 \end{bmatrix} \quad (39)$$

Since  $\bar{Q}$  is orthogonal,  $||\bar{Q}^T \bar{r}||_2 = ||\bar{r}||_2$ . Thus  $||\bar{r}||_2$  is minimized when

$$\bar{e}_1 = \bar{R}\sigma, \quad (40)$$

and when this is true

$$||\bar{r}||_2 = ||\bar{e}_2||_2 \quad (41)$$

It is important to realize that when  $k = \text{rank}(\bar{A}) = \min(M, N)$ , then the two subroutines DQRDC and DQRSL from LINPACK [21] provide the method for solving (30). DQRDC produces the QR decomposition of  $\bar{A}$  with column pivoting. This resulting matrix is passed to DQRSL for the solving stage. DQRSL uses the  $k = \text{rank}(\bar{A})$  columns to produce the desired least-squares fit.

If, however,  $\bar{A}$  is rank deficient (or near rank deficient), then we need a truncated least-squares fit. This can be achieved by using the subroutine DQRST [21, page 9.11]. This subroutine allows for a user supplied tolerance and calls DQRDC and DQRSL. Based on this tolerance, some of the columns of the output of DQRDC are zeroed. DQRSL then produces the truncated least-squares fit.

We apply the linearized theory that has just been described to (22), with the electric field column vector,  $\bar{E}$ , replaced by its zeroth order approximation,  $\bar{E}_0$ , so that the resulting equation becomes

$$EMF_k = (T_{kj} E_{0j}) \sigma_j \quad (42)$$

When we generated a singular-value decomposition of  $\bar{T}$ , we found that the ratio of the largest to smallest singular values was on the order of  $10^{12}$ . This ratio is a measure of the condition of the matrix. Thus, while we were working with a highly ill-conditioned matrix, our model produced very accurate results for inversion, as we will show in the next section.

We have pointed out before that our model equations, (8)-(11), or their discretized versions, (17)-(23), are in reality nonlinear. Thus, we must use a nonlinear least-squares scheme. The subroutines LMDER and LMSTR in MINPACK [22] fill this bill nicely. Both are based on the Levenberg-Marquardt method, which we briefly describe below [26, 27].

Recall our problem: (25)-(27). If we linearize, we see that

$$\|\bar{F}(\bar{\sigma} + \bar{p})\|_2 \approx \|\bar{F}(\bar{\sigma}) + \bar{F}'(\bar{\sigma})\bar{p}\|_2 = \psi(\bar{p}), \quad (43)$$

where  $\bar{F}'(\bar{\sigma})$  is the Jacobian matrix. A standard way of minimizing  $\psi(\bar{p})$  is by using a Gauss-Newton method:

$$\text{given: } \bar{\sigma}^{(k)}, \bar{F}(\bar{\sigma}^{(k)}), \bar{J}(\bar{\sigma}^{(k)}) = \bar{F}'(\bar{\sigma}^{(k)})$$

$$\text{solve: } \bar{J}(\bar{\sigma}^{(k)}) \bar{p}^{(k)} = -\bar{F}(\bar{\sigma}^{(k)}) \quad \text{in a least-squares sense}$$

$$\text{then let: } \bar{\sigma}^{(k+1)} = \bar{\sigma}^{(k)} + \bar{p}^{(k)}$$

This works well if  $\bar{J}(\bar{\sigma})$  is full rank. In the rank deficient, or nearly rank deficient case, however, modifications are required. It should be noted that in practice rank deficiency arises often.

Since the linearization of (43) is not valid globally, we consider a constrained linear least-squares problem:

$$\min_{\bar{p}} \{ \psi(\bar{p}) : ||\bar{D}\bar{p}||_2 \leq \Delta \} = \min_{\bar{p}} \{ ||\bar{F} + \bar{J}\bar{p}||_2 : ||\bar{D}\bar{p}||_2 \leq \Delta \} , \quad (44)$$

where  $\bar{D}$  is diagonal. The Levenberg-Marquardt method is based on the fact [26] that if  $\bar{p}^*$  is a solution to (44), then  $\bar{p}^* = \bar{p}(\lambda)$ , for some  $\lambda \geq 0$ , where:

$$(\bar{J}^T \bar{J} + \lambda \bar{D}^T \bar{D}) \bar{p} = -\bar{J}^T \bar{F} . \quad (45)$$

The way to solve for  $\bar{p}$  is to recognize that (45) are the normal equations for the linear least-squares problem

$$\begin{bmatrix} \bar{J} \\ \lambda^{1/2} \bar{D} \end{bmatrix} \bar{p} = - \begin{bmatrix} \bar{F} \\ \bar{0} \end{bmatrix} . \quad (46)$$

The implementation of these facts is the basis of the nonlinear least-squares subroutines in MINPACK.

In order to apply the nonlinear least-squares algorithm to our discretized model, we must send to LMDER and LMSTR the nonlinear function to be minimized, as well as the Jacobian. The Jacobian is obtained from (22) as

$$J_{kj} = T_{kj} E_j , \quad (47)$$

which is the matrix that multiplies the column vector  $\bar{0}$ . Therefore, the steps to be followed in solving the nonlinear least-squares problem are:

- enter initial guess for  $\bar{0}$  and solve (17) for  $\bar{E}$
- compute Jacobian from (47)
- compute  $\overline{EMF}_{model}$  from (22)
- form  $\bar{F}(\bar{0}) = \overline{EMF}_{model} - \overline{EMF}_{measured}$
- call LMDER or LMSTR

#### IV. EXAMPLES OF RECONSTRUCTION OF SIMULATED FLAWS

The theory of inversion involves two components, a theoretical model that is based on a rigorous application of electromagnetic theory, and numerical algorithms that effectively implement least-squares theory. Each of these has been dealt with, and now we illustrate how the method works for the reconstruction of computer simulated flaws.

All numerical experiments were run in double precision on the PRIME 550-II and IBM 360 machines. The double precision data word on the PRIME occupies 64 bits, of which 47 are the mantissa and 16 the exponent. The effective precision is about 14 digits. The IBM double precision word has a 56 bit mantissa, which allows an effective precision of about 17 digits. Precisions such as these are required for meaningful computations, because the condition number of the Jacobian matrix is phenomenal--on the order of  $10^{12}$ . Even with this large condition number, the computations produced excellent results; in the worst case the reconstructions were exact to at least three places on the PRIME, and five places on the IBM. This verifies that the algorithms in the LINPACK and MINPACK packages tend to work better in higher precision.

The physical system that was modeled is a variation of the multi-coil system that has been described earlier, and is shown in Figure 6. It consists of a fixed exciting coil and a single probe coil that can be moved axially. This system is typical of a common flaw detection scheme. The mesh on which the discretization is defined is also shown. It consists of six rows of ten cells, and spans the entire tube wall-thickness. The starting position of the probe coil is at the left edge of the mesh, and the final position is at the right edge. The probe coil is stepped through fifty equal intervals between these limits, thereby generating a total of 100 real and imaginary EMF values that are used in the least-squares inversion.

The physical parameters of the model are typical of real systems. The inner radius of the tube is 0.510", and the outer radius, 0.375". The length of the mesh is 0.50" in the z-direction, thereby giving a cell resolution of 0.05" by 0.011". The probe coil's inner radius is 0.05", outer radius, 0.100", and its length is 0.50", the same as the

mesh. The exciting coil is centered on the mesh in the z-direction (neither of these last two items is a requirement of the inversion method). The density of turns of the exciting coil is  $2 \times 10^6$  turns/m, which is comparable to that of 20 gauge copper wire. The probe coil has an inner radius of 0.100", outer radius of 0.26", and a length of 0.250". Its turns density is  $2 \times 10^7$  turns/m, which is comparable to 30 gauge copper wire. The tube conductivity is  $3.5 \times 10^7$ , which is equal to the conductivity of aluminum, and the frequency of operation is 1kHz.

In Figure 7 we show a simulated flaw (the "original") at the top and its reconstructed version at the bottom. The real (R) and imaginary (I) parts of the perturbed EMF, as measured by the probe coil when it is moved across the mesh, are shown in the middle of the figure. This EMF curve is actually an interpolation based on the fifty probe coil positions. In this figure, and the next two, we simulate the flaw by letting  $\sigma_f = 0$  at the flaw location, and  $\sigma_f = \sigma_0$  off of the flaw. Thus, according to (12)(b),  $\sigma_j = -1$  if the jth cell lies on the flaw, and  $\sigma_j = 0$ , otherwise.

Note, in Figure 7, that because the original flaw is placed symmetrically in the mesh, the EMF is symmetrical about the center of the mesh, also. The reconstruction is clearly perfect (to at least three significant digits), indicating that the least-squares inversion algorithms work quite well in this model. We must be careful to note, however, that in this report we have considered only original flaws that are defined on the same mesh as that used for reconstruction; i.e., each part of the flaw is constant over a full cell of the reconstruction mesh. We intend to consider the more general case, in which the flaw may be defined on a different mesh than that used for reconstruction (say, one with smaller cells, or cells that are displaced from the cells of the reconstruction mesh). This will test the ability of the model to resolve, as well as invert, data.

To satisfy ourselves that the excellent results that were obtained in Figure 7 were not due to symmetry, we considered the asymmetrical flaws of Figures 8 and 9. Again, the reconstruction was perfect to at least three significant digits. It should be noted from these three examples that the more concentrated the flaw, the greater is the peak of the EMF curve.

A crucial test of inversion in highly ill-conditioned systems has to do with corrupted data. The question is, does the reconstruction "follow" the corrupted data, or does the result lose all significant figures? In order to test our model's response to corrupted data, we performed the following numerical experiment. We assigned to each cell in the mesh a number between 0 and 1, chosen at random by using the FORTRAN random number generator. Then the model EMF that is produced by this "flaw" is computed by following the first three steps that are listed below (47). This "true" data is then corrupted by adding to it the same data multiplied by either 0.01, 0.10, or 0.20, and then using this as the "measured" EMF (see the discussion following (47)). Figure 10 shows the results of this experiment. There we show the original flaw, consisting of the sixty randomly chosen cell conductivities, followed by the reconstructed flaw, simulated by the sixty values of computed cell conductivities, for the case of 1%, 10%, and 20% corrupted data.

Again, the results are excellent. We don't, of course, expect to reconstruct the original flaw by using corrupted EMF data. We are happy, though, to see that the reconstructed flaw "tracks" the original flaw, in the sense that it departs by almost exactly 1%, 10%, or 20% from the original. Such stability in the face of a very ill-conditioned system attests to the excellence of the LINPACK and MINPACK algorithms.

The same results that are shown in Figures 7-10, are obtained with either the linear or nonlinear algorithms that are described in Section III. The reason for this is that in (17) the term involving the matrix  $\bar{G}$  is much smaller than the first term,  $\bar{A}$ . Thus, the solution of the equation is  $E \approx E_0$ , and when this is substituted into (22), or (47), we see that the Jacobian matrix is constant, so that the nonlinear algorithms may be replaced by the simpler linear ones.

## V. COMMENTS AND CONCLUSIONS

In this report we have developed a model for eddy-current inversion that is based on the application of rigorous electromagnetic theory and numerical algorithms for least-squares. So far we have attempted only

to verify the inversion method for flaws that were defined on the same grid as that used for reconstruction. The results have been excellent, and suggest that the method can be used as the basis for the development of an engineering prototype system. Before such a system can be effected, however, we believe that the following additional studies should be carried out:

- study resolution of flaws that are defined on a different grid than that used for reconstruction
- carry out examples of reconstruction in the presence of known irregularities
- determine computer hardware requirements
- determine computer software requirements
- determine relative advantages of multicoil, multi-frequency, and transient (time-domain) systems
- optimize exciting coil and probe configurations and design.

## VI REFERENCES

- [1] F. Forster and H. Breitfeld, "Theoretische und Experimentelle Grundlagen der zerstörungsfreien Werkstoffprüfung mit Wirbelstromverfahren," Parts I and II, Z. Metallkunde, Vol. 43, No. 5, 1952, pp. 163-180;  
F. Forster, H. Breitfeld and K. Stambke, "Theoretische und Experimentelle Grundlagen der zerstörungsfreien Werkstoffprüfung mit Wirbelstromverfahren," Parts III-VII, Z. Metallkunde, Vol. 43, No. 5, 1954, pp. 166-199 and 221-226.
- [2] M. L. Burrows, "A Theory of Eddy-Current Flaw Detection," thesis, University of Michigan, 1964; available from University Microfilms, Inc., Ann Arbor, MI.

- [3] C. V. Dodd and W. E. Deeds, "Analytical Solutions to Eddy-Current Probe Coil Problems," J. Appl. Phys., 39, 2829-2838.
- [4] J. W. Luquire, W. E. Deeds and C. V. Dodd, "Alternating Current Distribution Between Planar Conductors," J. Appl. Phys., 41, 3983-3991.
- [5] C. C. Cheng, C. V. Dodd and W. E. Deeds, "General Analysis of Probe Coils Near Stratified Conductors," Int. J. Nondestructive Testing, 3, 109-130 (1971).
- [6] C. W. Nestor, Jr., C. V. Dodd and W. E. Deeds, "Analysis and Computer Programs for Eddy Current Coils Concentric with Multiple Cylindrical Conductors," Report No. ORNL-5220, Oak Ridge National Laboratory, Oak Ridge, TN 37830, July 1979.
- [7] W. E. Deeds, C. V. Dodd and G. W. Scott, "Computer-Aided Design of Multifrequency Eddy-Current Tests for Layered Conductors with Multiple Property Variations," Report No. ORNL/TM-6858, Oak Ridge National Laboratory, Oak Ridge, TN 37830, October 1979.
- [8] Nondestructive Evaluation Program: Progress in 1979, EPRI NP-1234-SR, Electric Power Research Institute, Palo Alto, CA 94304, December 1979.
- [9] Special Issue on Inverse Methods in Electromagnetics, IEEE Transactions on Antennas and Propagation, Vol. AP-29, No. 2, March 1981.
- [10] P. C. Sabatier, ed., Applied Inverse Problems, Vol. 85, Lecture Notes in Physics, Springer-Verlag, Berlin, 1978.
- [11] H. P. Baltes, ed., Inverse Scattering Problems in Optics, Vol. 20, Topics in Current Physics, Springer-Verlag, Berlin, 1980.
- [12] W. E. Glenn, J. Ryu, S. H. Ward, W. J. Peeples and R. J. Phillips, "The Inversion of Vertical Magnetic Dipole Sounding Data," Geophysics, 38, No. 6 (Dec. 1973), pp. 1109-1129.
- [13] J. R. Inman, Jr., J. Ryu and S. H. Ward, "Resistivity Inversion," Geophysics, 38, No. 6 (Dec. 1973), pp. 1088-1108.
- [14] D. D. Jackson, "Interpretation of Inaccurate, Insufficient and Inconsistent Data," Geophys. J. R. Astr. Soc. (1972) 28, pp. 97-109.
- [15] D. L. B. Jupp and K. Vozoff, "Stable Iterative Methods for the Inversion of Geophysical Data," Geophys. J. R. Astr. Soc. (1975) 42, pp. 957-976.

- [16] M. L. Oristaglio and M. H. Worthington, "Inversion of Surface and Borehole Electromagnetic Data for Two-Dimensional Electrical Conductivity Models," Geophysical Prospecting, 1980, 28, 633-657.
- [17] S. H. Ward, W. J. Peeples and J. Fvu, "Analysis of Geoelectromagnetic Data," in Methods in Computational Physics, Geophysics, 13, 163-236.
- [18] P. Weidelt, "Inversion of Two-Dimensional Conductivity Structures," Physics of the Earth and Plantetary Interiors, 10 (1975), 282-291.
- [19] Special Issue on Applications of Electromagnetic Theory to Geophysical Exploration, Proc. IEEE, Vol. 67, No. 7, July 1979.
- [20] H. Libby, Introduction to Electromagnetic Nondestructive Test Methods, Chapters 7 and 8, Wiley-Interscience, New York, 1971.
- [21] J. J. Dongarra, J. R. Bunch, C. B. Moler and G. W. Stewart, LINPACK Users' Guide, Society for Industrial and Applied Mathematics, Philadelphia, 1979.
- [22] Jorge J. Moré, Burton S. Garbow and Kenneth E. Hillstom, "User Guide for MINPACK-1," Report No. ANL-80-74, Argonne National Laboratory, 9700 South Cass Avenue, Argonne, IL 60439, August 1980.
- [23] C. T. Tai, Dyadic Green's Functions in Electromagnetic Theory, International Textbook Company, Scranton, 1971.
- [24] Roger F. Harrington, Field Computation by Moment Methods, The Macmillan Company, New York, 1968.
- [25] G. W. Stewart, Introduction to Matrix Computations, Academic Press, New York, 1973.
- [26] J. J. Moré, The Levenberg-Marquardt Algorithm: Implementation and Theory, Lecture Notes in Mathematics, Vol. 630, Springer-Verlag, Berlin, 1977.
- [27] J. E. Dennis, Jr., "Non-Linear Least Squares and Equations," in Conference on the State of the Art in Numerical Analysis, D. A. Jacobs, ed., Academic Press, New York, 1976.

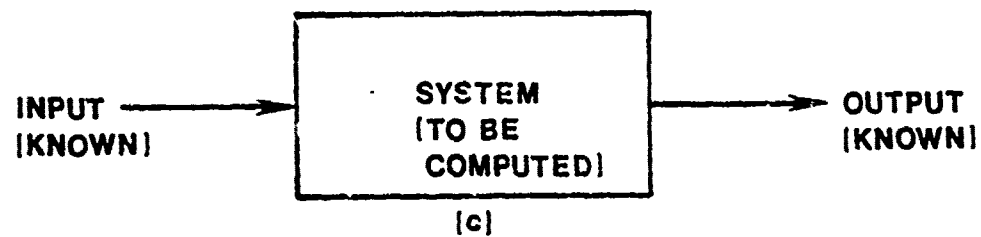
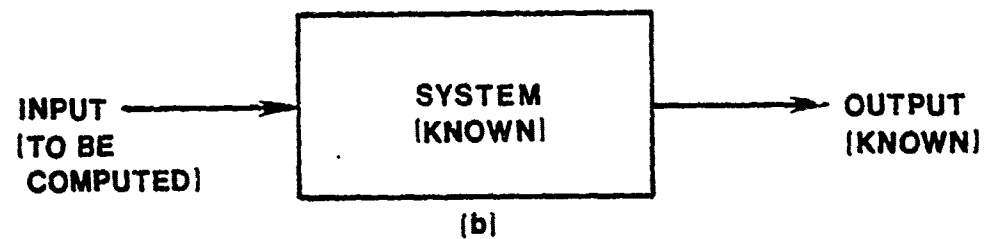
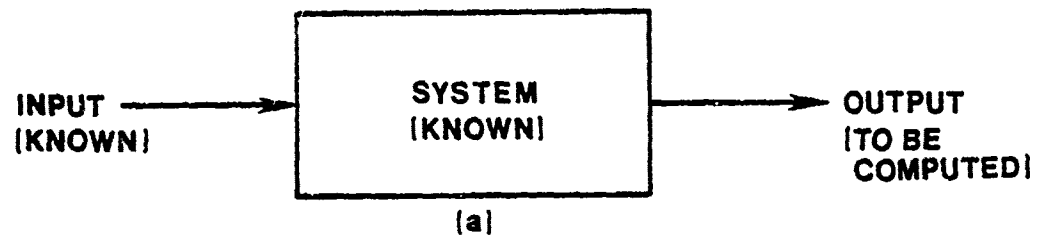


Figure 1. Illustrating three systems problems: (a) the "direct" problem, (b) the "signal-detection" problem, and (c) the "inverse" system-identification problem.

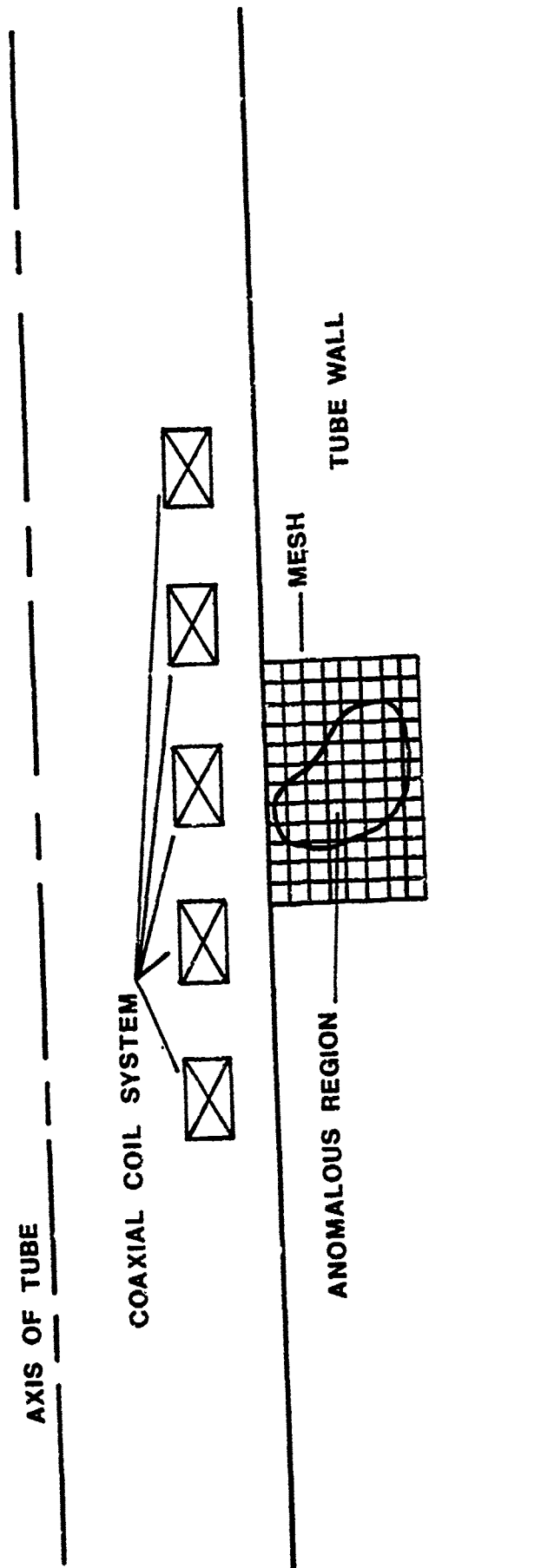


Figure 2. Illustrating a multicoil system for inverting data defined on the mesh, in order to reconstruct the anomalous region.

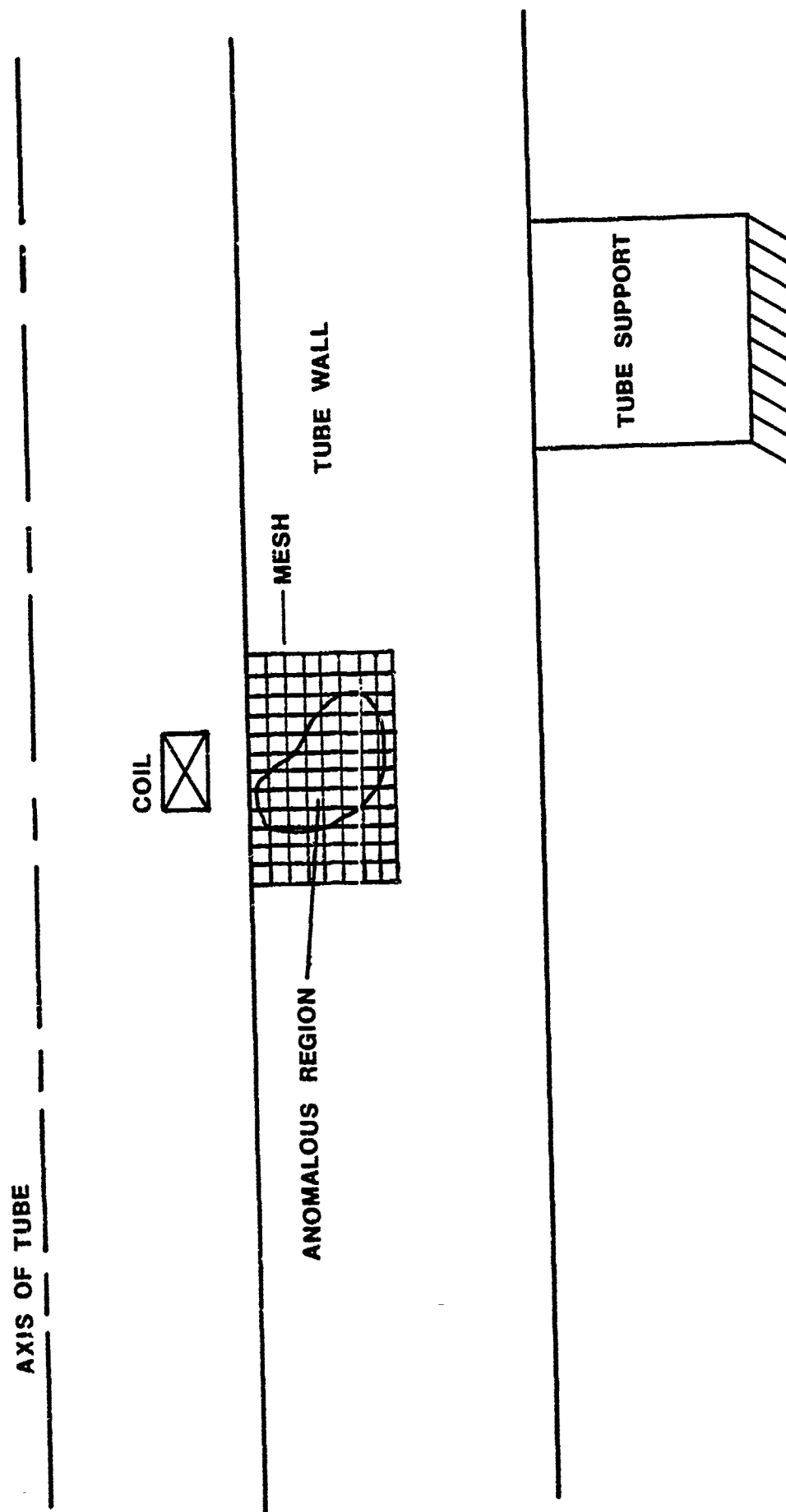


Figure 3. Illustrating the detection of flaws in the presence of a tube support, or other known irregularity.

AXIS OF TUBE

COIL

ANOMALOUS  
REGION

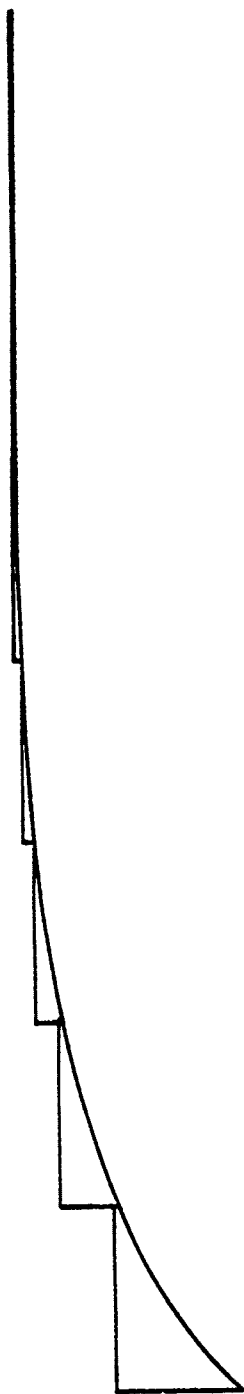
MESH

THESE CHANGES IN  
RADIi ARE KNOWN

TUBE WALL

Figure 4. Illustrating the detection of flaws in a tube whose inner and/or outer diameters vary in a known manner.

(a)



(b)

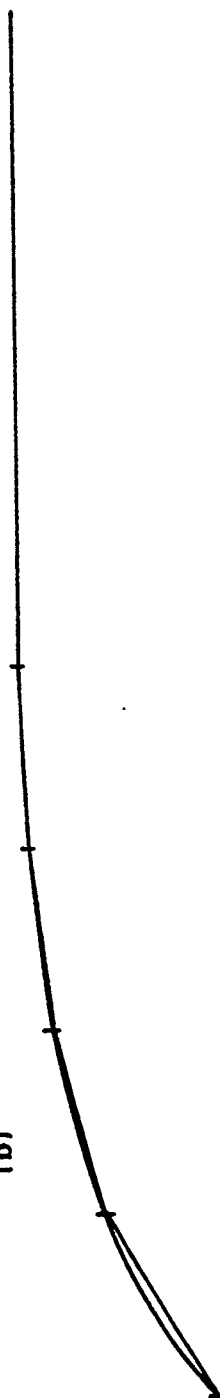


Figure 5. Illustrating the approximation of a curved surface by splines of (a) zero order and (b) first order.

AXIS OF TUBE

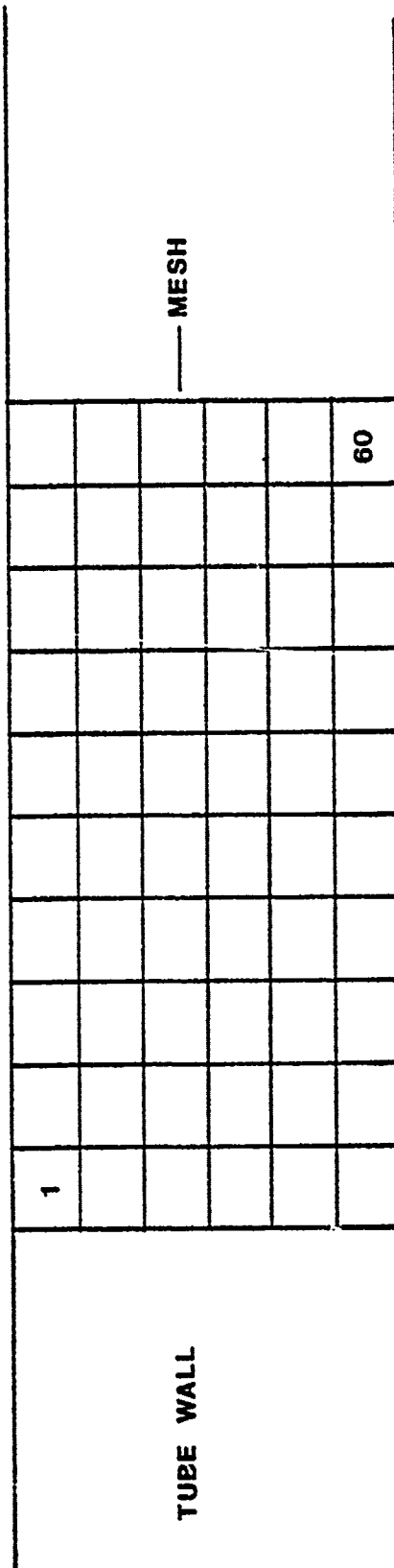
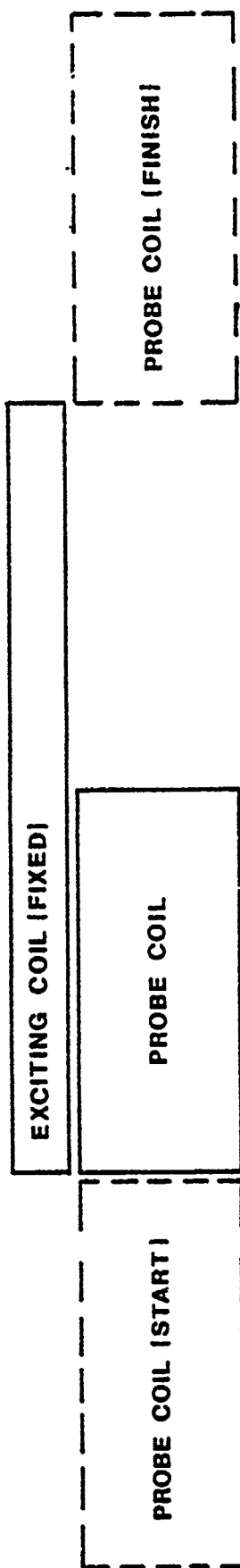


Figure 6. Illustrating the system for which results have been computed. It consists of a fixed exciting coil and a single probe coil that can be moved axially across the mesh.

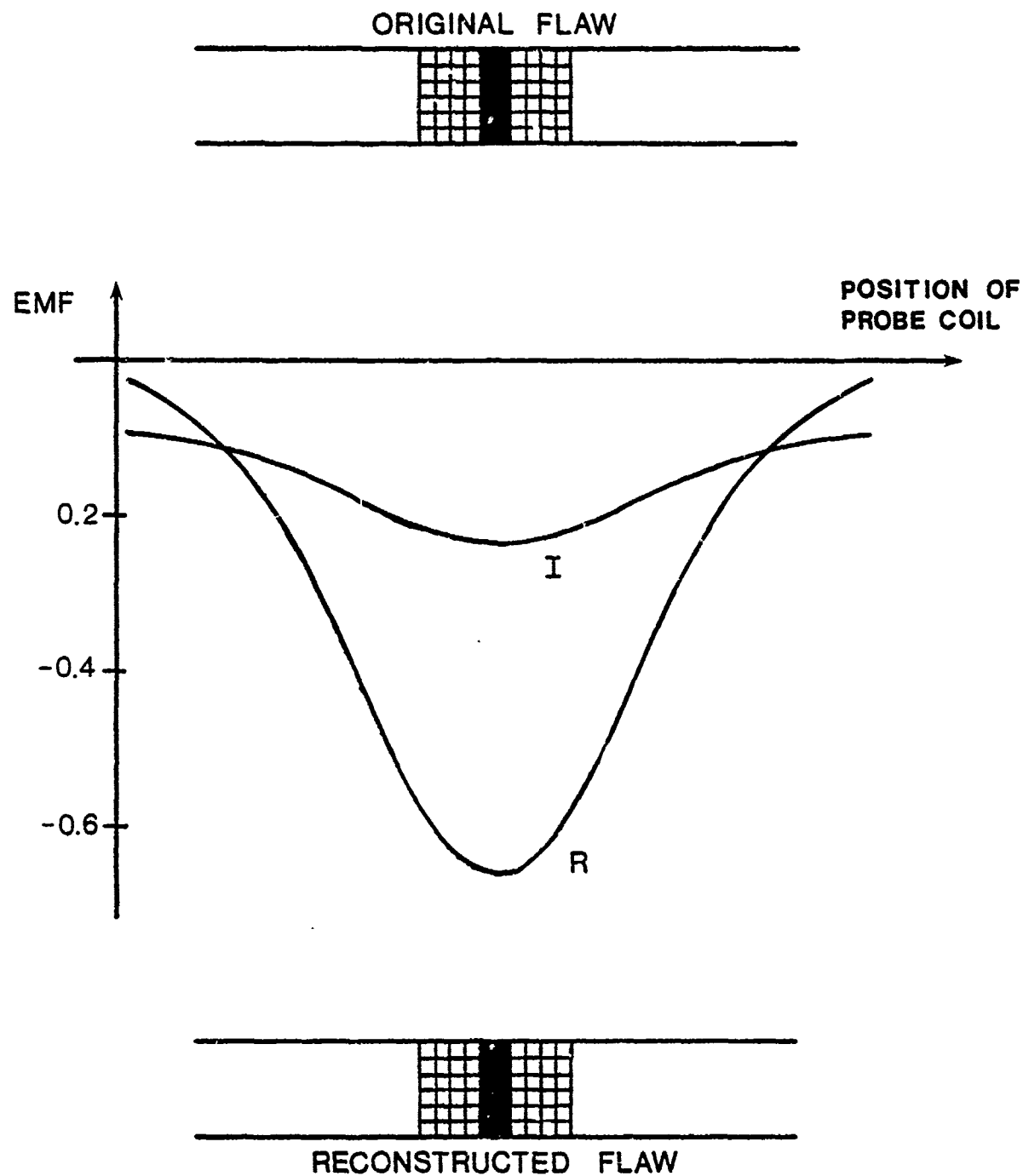


Figure 7. Illustrating a symmetrically placed flaw (top), the real (R) and imaginary (I) parts of the EMF induced into the probe coil (center), and the reconstructed flaw (bottom). The flaw consists of the darkened cells. The reconstruction is exact to the least three significant digits.

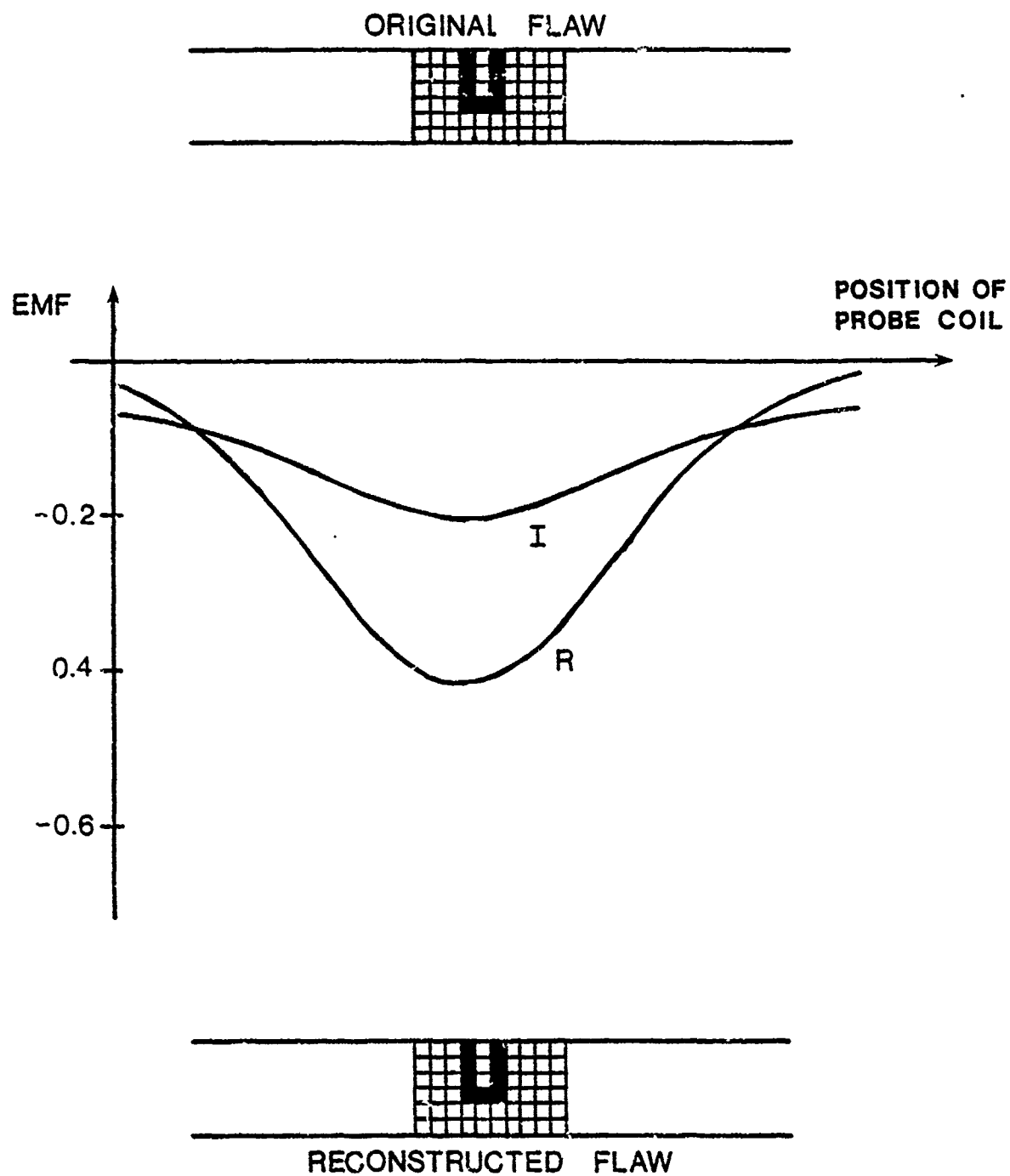


Figure 8. Illustrating the reconstruction of an asymmetrically placed flaw. The interpretation of the figure is the same as of Figure 7.

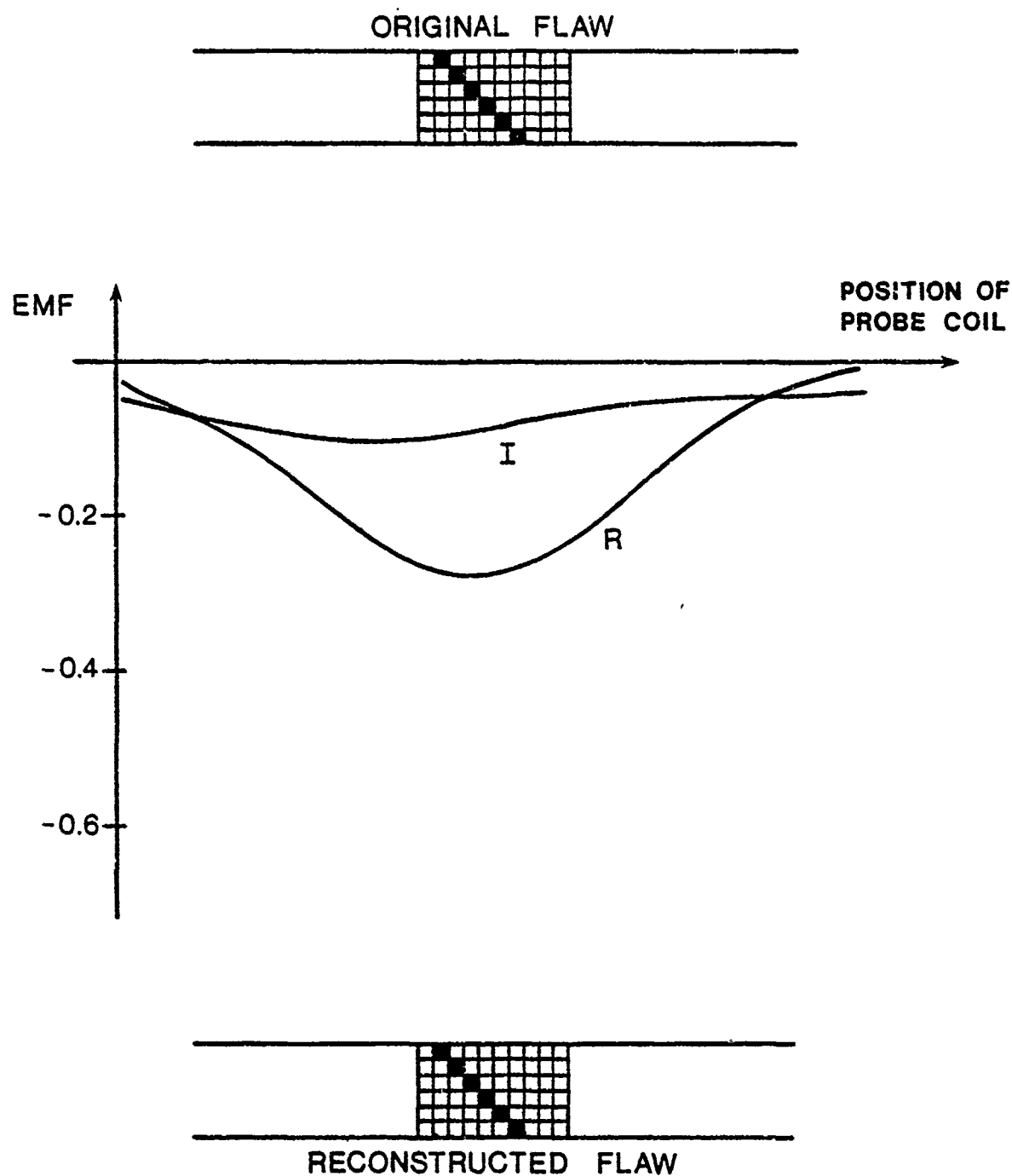


Figure 9. Illustrating the reconstruction of another asymmetrically placed flaw.

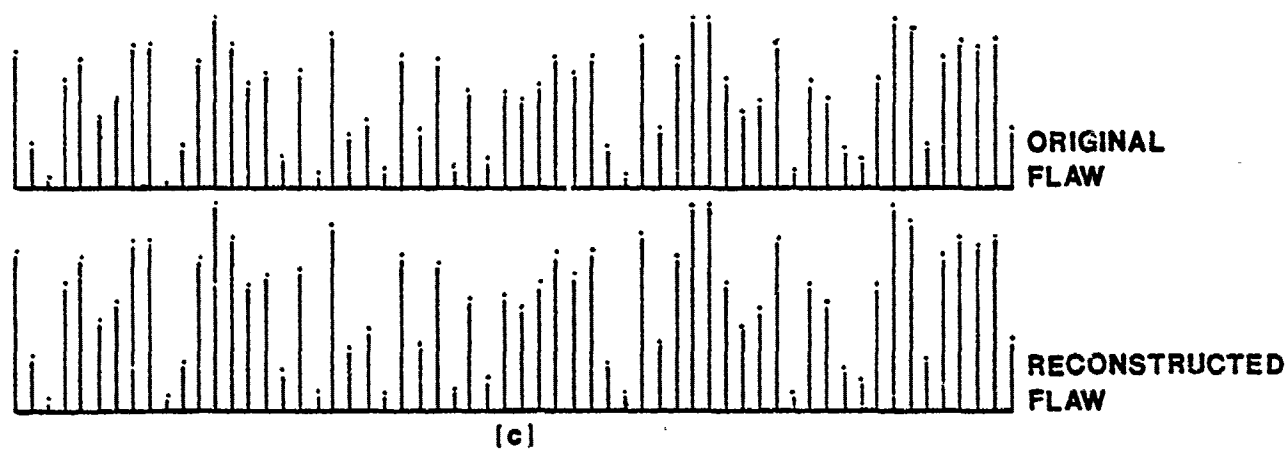
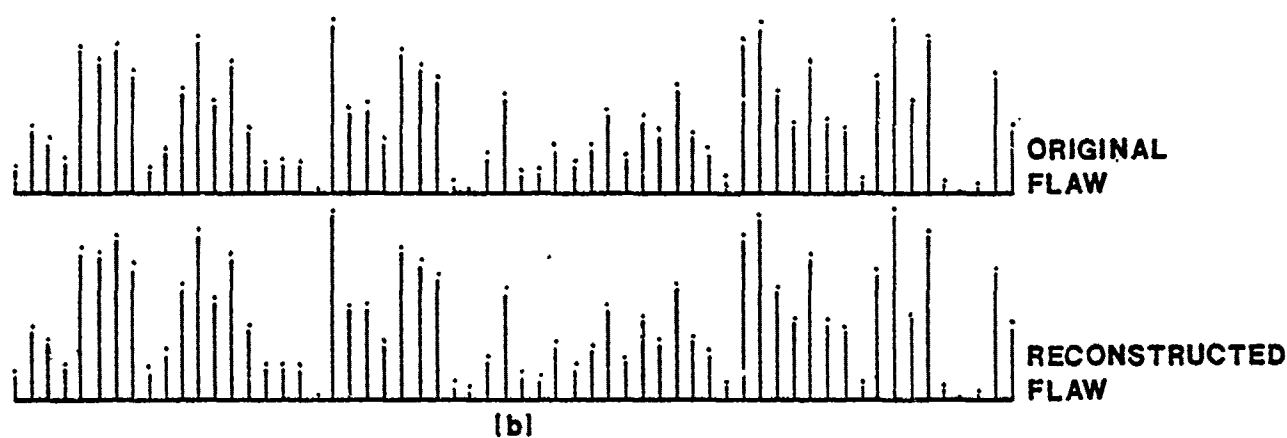
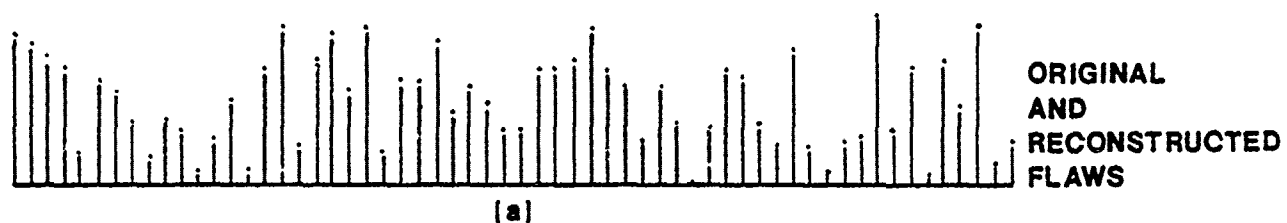


Figure 10. Illustrating the reconstruction of random flaws with perturbed EMF data: (1) 1% perturbation, (b) 10% perturbation, (c) 20% perturbation.

# APPENDIX A. CALCULATION OF THE GREEN'S FUNCTION

The interest of the cylinder is labeled region 1, the tube wall, region 2, and the exterior to the cylinder, region 3. In each region the magnetic permeability is  $\mu_0$  and the dielectric constant,  $\epsilon_0$ . The electrical conductivity of regions 1 and 3 is zero, whereas that for region 2 is  $\sigma$ . We use the notion

$G_{ij}(r, z; r', z')$  = field produced at  $(r, z)$  in region  $i$ .  
due to a filamentary current loop at  
 $(r', z')$  in region  $j$ , where  $i, j = 1, 2, 3$ .

Using this notation, the Green's function satisfies

$$\nabla \times \nabla \times \bar{G}_{11} - k_1^2 \bar{G}_{11} = \frac{\delta(r-r')\delta(z-z')}{2\pi r'} \bar{a}_\phi \quad (A-1)(a)$$

$$\nabla \times \nabla \times \bar{G}_{21} - k_2^2 \bar{G}_{21} = 0 \quad (b)$$

$$\nabla \times \nabla \times \bar{G}_{31} - k_3^2 \bar{G}_{31} = 0 \quad (c)$$

$$\nabla \times \nabla \times \bar{G}_{12} - k_1^2 \bar{G}_{12} = 0 \quad (A-2)(a)$$

$$\nabla \times \nabla \times \bar{G}_{22} - k_2^2 \bar{G}_{22} = \frac{\delta(r-r')\delta(z-z')}{2\pi r'} \bar{a}_\phi \quad (b)$$

$$\nabla \times \nabla \times \bar{G}_{32} - k_3^2 \bar{G}_{32} = 0 \quad (c)$$

$$\nabla \times \nabla \times \bar{G}_{13} - k_1^2 \bar{G}_{13} = 0 \quad (A-3)(a)$$

$$\nabla \times \nabla \times \bar{G}_{23} - k_2^2 \bar{G}_{23} = 0 \quad (b)$$

$$\nabla \times \nabla \times \bar{G}_{33} - k_3^2 \bar{G}_{33} = \frac{\delta(r-r')\delta(z-z')}{2\pi r'} \bar{a}_\phi \quad (c)$$

where  $k_{1,3}^2 = k_0^2 = \omega^2 \mu_0 \epsilon_0$ ,  $k_2^2 = \omega^2 \mu_0 \epsilon_0 - j\omega \mu_0 \sigma$ .

If we write  $\bar{G}_{ij} = G_{ij} \bar{a}$ , where the scalar  $G_{ij}$  is independent of  $\phi$ , because the vector  $\bar{G}_{ij}$  is divergenceless, then the vector differential operator on the left-hand side of these equations is replaced by the scalar differential operator

$$\frac{\partial^2 G_{ij}}{\partial z^2} + \frac{\partial^2 G_{ij}}{\partial r^2} + \frac{1}{r} \frac{\partial G_{ij}}{\partial r} - \frac{G_{ij}}{r^2} + k^2 G_{ij} = 0, \quad (A-4)$$

where  $k$  stands for either  $k_0$  or  $k_2$ .

The only parts of the Green's function that are required in the model equations, (8)-(11), are  $G_{12}$ ,  $G_{22}$ , and  $G_{21}$ ; but  $G_{21}(r', z'; r, z) = G_{12}(r, z; r', z')$  because  $\mu = \mu_0$  in each of the three regions (see [23] of the main text). Hence, all we need be concerned with is (A-2), which we rewrite using (A-4):

$$\frac{\partial^2 G_{12}}{\partial z^2} + \frac{\partial^2 G_{12}}{\partial r^2} + \frac{1}{r} \frac{\partial G_{12}}{\partial r} - \frac{G_{12}}{r^2} + k_0^2 G_{12} = 0 \quad (A-5)(a)$$

$$\frac{\partial^2 G_{22}}{\partial z^2} + \frac{\partial^2 G_{22}}{\partial r^2} + \frac{1}{r} \frac{\partial G_{22}}{\partial r} - \frac{G_{22}}{r^2} + k_2^2 G_{22} = - \frac{\delta(r-r')\delta(z-z')}{2\pi r'} \quad (b)$$

$$\frac{\partial^2 G_{32}}{\partial z^2} + \frac{\partial^2 G_{32}}{\partial r^2} + \frac{1}{r} \frac{\partial G_{32}}{\partial r} - \frac{G_{32}}{r^2} + k_0^2 G_{32} = 0 \quad (c)$$

We use Fourier transforms to solve (A-5). Thus,

$$G_{12}(r, z; r', z') = \int_{-\infty}^{\infty} \tilde{G}_{12}(r, h; r') e^{-jh(z-z')} dh, \quad (A-6)$$

so that (A-5) becomes

$$\begin{aligned} \int_{-\infty}^{\infty} \left( \frac{d^2 \tilde{G}_{12}}{dr^2} + \frac{1}{r} \frac{d\tilde{G}_{12}}{dr} - \frac{\tilde{G}_{12}}{r^2} + (k_1^2 - h^2) \tilde{G}_{12} \right) e^{-jh(z-z')} dh \\ = -\delta_{12} \frac{\delta(r-r')}{(2\pi)^2 r'} \int_{-\infty}^{\infty} e^{-jh(z-z')} dh, \end{aligned} \quad (A-7)$$

where we have used the completeness relation

$$\delta(z - z') = \frac{1}{2\pi} \int_{-\infty}^{\infty} e^{-jh(z-z')} dh, \quad (\text{A-8})$$

and  $\delta_{ij} = 1$ , if  $i = j$ , and  $= 0$ , otherwise.

Since (A-7) holds for all,  $z, z'$ , we can equate integrands to get the differential equation that is satisfied by the transformed variable:

$$\frac{d^2 \tilde{G}_{i2}}{dr^2} + \frac{1}{r} \frac{d\tilde{G}_{i2}}{dr} - \frac{\tilde{G}_{i2}}{r^2} + (k_i^2 - h^2) \tilde{G}_{i2} = - \frac{\delta(r-r')}{(2\pi)^2 r'} \delta_{i2} \quad (\text{A-9})$$

Let  $r_1$  be the inner radius of the cylinder and  $r_2$ , the outer. Then the boundary conditions that are to be satisfied by the  $G_{i2}$  are:

$$\tilde{G}_{n2}(r_n) = \tilde{G}_{n+1,2}(r_n), \quad n = 1, 2 \quad (\text{A-10})(a)$$

$$\frac{d\tilde{G}_{n2}(r_n)}{dr} + \frac{\tilde{G}_{n2}(r_n)}{r} = \frac{d\tilde{G}_{n+1,2}(r_n)}{dr} + \frac{\tilde{G}_{n+1,2}(r_n)}{r}, \quad n = 1, 2 \quad (b)$$

$$\tilde{G}_{22}(r'_-) = \tilde{G}_{22}(r'_+) \quad (c)$$

$$\frac{d\tilde{G}_{22}(r'_+)}{dr} + \frac{\tilde{G}_{22}(r'_+)}{r} - \frac{d\tilde{G}_{22}(r'_-)}{dr} - \frac{\tilde{G}_{22}(r'_-)}{r} = \frac{-1}{4\pi^2 r'} \quad (d)$$

Equations (A-10)(a),(b) imply the continuity of tangential electric and magnetic field, respectively, across a surface that does not carry magnetic or electric current singularities. Equation (A-10)(d), on the other hand, implies that the tangential component of magnetic field intensity suffers a discontinuity of amount  $-1/4\pi r'$  in crossing the surface  $r = r'$ , on which the filamentary current source resides. Alternatively, (A-10)(b),(d) can be obtained by integrating (A-9) an infinitesimal distance across the surfaces  $r = r_1, r = r_2$  or  $r = r'$ , and then invoking the continuity of electric field, as expressed in (A-10)(a),(c), across these same surfaces.

Because the source point,  $r = r'$ , is in region 2, we have the following solutions of (A-9):

$$\tilde{G}_{12} = AJ_1(\alpha_0 r), \quad r \leq r_1, \quad \alpha_0 = (k_0^2 - h^2)^{1/2} \quad (\text{A-11})(a)$$

$$\tilde{G}_{22} = BH_1^{(1)}(\alpha_1 r) + CH_1^{(2)}(\alpha_1 r), \quad r_1 \leq r < r', \quad \alpha_1 = (k_2^2 - h^2)^{1/2} \quad (b)$$

$$\tilde{G}_{22} = DH_1^{(1)}(\alpha_1 r) + EH_1^{(2)}(\alpha_1 r), \quad r' < r \leq r_2 \quad (c)$$

$$\tilde{G}_{32} = FH_1^{(2)}(\alpha_0 r), \quad r \geq r_2, \quad (d)$$

where A-F are arbitrary constants that are chosen to satisfy the boundary conditions (A-10).

We use the Bessel function  $J_1$  in region 1, because that region includes the z-axis,  $r = 0$ , and  $J_1$  is regular there. The Hankel function,  $H_1^{(2)}$ , is used in region 3, because that region extends to  $r = \infty$ , and  $H_1^{(2)}$  is regular there (that is  $H_1^{(2)}$  represents an outgoing cylindrical wave at infinity).

The six constants, A-F, are determined by applying (A-10) to (A-11), with the result:

$$AJ_1(\alpha_0 r_1) = BH_1^{(1)}(\alpha_1 r_1) + CH_1^{(2)}(\alpha_1 r_1) \quad (\text{A-12})(a)$$

$$\alpha_0 AJ_0(\alpha_0 r_1) = \alpha_1 BH_0^{(1)}(\alpha_1 r_1) + \alpha_1 CH_0^{(2)}(\alpha_1 r_1) \quad (b)$$

$$BH_1^{(1)}(\alpha_1 r') + CH_1^{(2)}(\alpha_1 r') = DH_1^{(1)}(\alpha_1 r') + EH_1^{(2)}(\alpha_1 r') \quad (c)$$

$$\alpha_1 BH_0^{(1)}(\alpha_1 r') + \alpha_1 CH_0^{(2)}(\alpha_1 r') = \alpha_1 DH_0^{(1)}(\alpha_1 r') + \alpha_1 EH_0^{(2)}(\alpha_1 r') + \frac{1}{4\pi^2 r'} \quad (d)$$

$$DH_1^{(1)}(\alpha_1 r_2) + EH_1^{(2)}(\alpha_1 r_2) = FH_1^{(2)}(\alpha_0 r_2) \quad (e)$$

$$\alpha_1 DH_0^{(1)}(\alpha_1 r_2) + \alpha_1 EH_0^{(2)}(\alpha_1 r_2) = \alpha_0 FH_0^{(2)}(\alpha_0 r_2) \quad (f)$$

In arriving at the final form of these equations, we used the Bessel function identity  $dB_1/dz + B_1/z = B_0$ , where B stands for J,  $H^{(1)}$ ,  $H^{(2)}$ .

These equations can be solved in a straightforward manner, and the constants then substituted back into (A-11). The results are:

$$\tilde{G}_{12}(r, h; r') = \frac{v_1 H_1^{(1)}(\alpha_1 r') + v_2 H_1^{(2)}(\alpha_1 r')}{(2\pi)^2 r_1 (v_1 v_4 - v_2 v_3)} J_1(\alpha_0 r) \quad (A-13)(a)$$

$$\tilde{G}_{22}(r, h; r') = \frac{[v_1 H_1^{(1)}(\alpha_1 r') + v_2 H_1^{(2)}(\alpha_1 r')][v_3 H_1^{(1)}(\alpha_1 r) + v_4 H_1^{(2)}(\alpha_1 r)]}{-j16\pi(v_1 v_4 - v_2 v_3)},$$

$$r_1 \leq r < r' \quad (b)$$

$$\tilde{G}_{22}(r, h; r') = \frac{[v_3 H_1^{(1)}(\alpha_1 r') + v_4 H_1^{(2)}(\alpha_1 r')][v_1 H_1^{(1)}(\alpha_1 r) + v_2 H_1^{(2)}(\alpha_1 r)]}{-j16\pi(v_1 v_4 - v_2 v_3)},$$

$$r' < r \leq r_2 \quad (c)$$

$$\tilde{G}_{32}(r, h; r') = \frac{v_3 H_1^{(1)}(\alpha_1 r') + v_4 H_1^{(2)}(\alpha_1 r')}{(2\pi)^2 r_2 (v_1 v_4 - v_2 v_3)} H_1^{(2)}(\alpha_0 r), \quad (d)$$

where

$$v_1 = \alpha_1 H_1^{(2)}(\alpha_0 r_2) H_0^{(2)}(\alpha_1 r_2) - \alpha_0 H_0^{(2)}(\alpha_0 r_2) H_1^{(2)}(\alpha_1 r_2) \quad (A-14)(a)$$

$$v_2 = -\alpha_1 H_1^{(2)}(\alpha_0 r_2) H_0^{(1)}(\alpha_1 r_2) + H_0^{(2)}(\alpha_0 r_2) H_1^{(1)}(\alpha_1 r_2) \quad (b)$$

$$v_3 = \alpha_1 J_1(\alpha_0 r_1) H_0^{(2)}(\alpha_1 r_1) - \alpha_0 J_0(\alpha_0 r_1) H_1^{(2)}(\alpha_1 r_1) \quad (c)$$

$$v_4 = -\alpha_1 J_1(\alpha_0 r_1) H_0^{(1)}(\alpha_1 r_1) + \alpha_0 J_0(\alpha_0 r_1) H_1^{(1)}(\alpha_1 r_1) \quad (d)$$

Throughout the calculations, liberal use is made of the Wronskian relation

$$H_{n+1}^{(1)}(z) H_n^{(2)}(z) - H_n^{(1)}(z) H_{n+1}^{(2)}(z) = -j4/\pi z \quad .$$

The final integral expressions for the Green's function are obtained upon substituting (A-13) into (A-6):

$$G_{12}(r, z; r', z') = \int_{-\infty}^{\infty} \frac{v_1 H_1^{(1)}(\alpha_1 r') + v_2 H_1^{(2)}(\alpha_1 r')}{(2\pi)^2 r_1 (v_1 v_4 - v_2 v_3)} J_1(\alpha_0 r) e^{-jh(z-z')} dh \quad (A-15) (a)$$

$$G_{22}(r, z; r', z') =$$

$$\frac{j}{\pi} \int_{-\infty}^{\infty} \frac{[v_1 H_1^{(1)}(\alpha_1 r') + v_2 H_1^{(2)}(\alpha_1 r')] [v_3 H_1^{(1)}(\alpha_1 r) + v_4 H_1^{(2)}(\alpha_1 r)]}{(v_1 v_4 - v_2 v_3)} \quad .$$

$$\cdot e^{-jh(z-z')} dh, \quad r_1 \leq r < r' \quad (b)$$

$$G_{22}(r, z; r', z') =$$

$$\frac{1}{16\pi} \int_{-\infty}^{\infty} \frac{[V_3 H_1^{(1)}(\alpha_1 r') + V_4 H_1^{(2)}(\alpha_1 r')] [V_1 H_1^{(1)}(\alpha_1 r) + V_2 H_1^{(2)}(\alpha_1 r)]}{(V_1 V_4 - V_2 V_3)} \cdot e^{-jh(z-z')} dh, \quad r' < r \leq r_2 \quad (c)$$

$$G_{32}(r, z; r', z') = \int_{-\infty}^{\infty} \frac{V_3 H_1^{(1)}(\alpha_1 r') + V_4 H_1^{(2)}(\alpha_1 r')}{(2\pi)^2 r_2 (V_1 V_4 - V_2 V_3)} H_1^{(2)}(\alpha_0 r) e^{-jh(z-z')} dh \quad (d)$$

#### APPENDIX B. CALCULATION OF MATRIX ELEMENTS

In this appendix, we derive expressions for the forcing-function vector, (19)(c), and the matrices, (19)(b), and (23).

In order to compute (19)(c), we start with the reciprocity relation

$$G_{21}(r, z; r', z') = G_{12}(r', z'; r, z), \quad (B-1)$$

where the last equality follows from (A-15)(a). We assume then that the exciting coil occupies the region  $\rho_1^{(e)} \leq r \leq \rho_2^{(e)}$ ,  $z_1^{(e)} \leq z \leq z_2^{(e)}$ .

Then, when we substitute (B-1) into (19)(c), and interchange the order of integration, we get

$$F_i = \frac{-j\omega\mu_0 n_e I_e}{\pi r_1}$$

$$\int_{-\infty}^{\infty} \frac{e^{-jh(z_1 - \zeta^{(e)})} \sin(hL_e/2) I(\rho_2^{(e)} \alpha_0, \rho_1^{(e)} \alpha_0)}{h\alpha_0^2 (v_1 v_4 - v_2 v_3)} \cdot [v_1 H_1^{(1)}(\alpha_1 r_1) + v_2 H_1^{(2)}(\alpha_1 r_1)] dh, \quad (B-2)$$

where  $L_e$  is the length and  $\zeta^{(e)}$  the midpoint of the exciting coil, and

$$I(z_2, z_1) = \int_{z_1}^{z_2} J_1(\zeta) \zeta d\zeta. \quad (B-3)$$

Before computing (19)(b), we introduce the vector notation

$$\bar{v}_{12} \cdot \bar{H}_1 = v_1 H_1^{(1)} + v_2 H_1^{(2)}, \quad \bar{v}_{34} \cdot \bar{H}_1 = v_3 H_1^{(1)} + v_4 H_1^{(2)}.$$

In addition, we let  $r_>$  be the larger of  $(r_i, r')$ , where  $r_i$  is the radial midpoint of the  $i$ th cell, and  $r_<$  the smaller. Using this notation allows us to write (19)(b) concisely as

$$G_{ij} = \sigma_j \int_{r_j^-}^{r_j^+} \int_{z_j^-}^{z_j^+} G_{22}(r_i, z_i; r', z') r' dr' dz'$$

$$\begin{aligned}
&= \sigma_j \frac{j}{16\pi} \int_{-\infty}^{\infty} \left\{ \int_{z_j^-}^{z_j^+} e^{-jh(z_i - z')} dz' \int_{r_j^-}^{r_j^+} \frac{(\bar{v}_{12} \cdot \bar{H}_1(\alpha_1 r_>)) (\bar{v}_{34} \cdot \bar{H}_1(\alpha_1 r_<))}{(v_1 v_4 - v_2 v_3)} \right\} dh \\
&= \sigma_j \frac{j}{16\pi} \int_{-\infty}^{\infty} \left\{ \frac{e^{-jh(z_i - z_j^+)} - e^{-jh(z_i - z_j^-)}}{jh} \right. \\
&\quad \left. \int_{r_j^-}^{r_j^+} \frac{(\bar{v}_{12} \cdot \bar{H}_1(\alpha_1 r_>)) (\bar{v}_{34} \cdot \bar{H}_1(\alpha_1 r_<))}{(v_1 v_4 - v_2 v_3)} r' dr' \right\} dh \tag{B-4}
\end{aligned}$$

In order to evaluate the inner integral we must consider three cases: (i)  $r_i < r_j^-$ , (ii)  $r_i = r_j$ , and (iii)  $r_i > r_j^+$ . In (i), clearly  $r_< = r_i$ ,  $r_> = r'$ , and in (iii)  $r_< = r'$ ,  $r_> = r_i$ . Hence, the inner integral above can be immediately computed for these two cases:

$$\begin{aligned}
&\int_{r_j^-}^{r_j^+} \frac{(\bar{v}_{12} \cdot \bar{H}_1(\alpha_1 r')) (\bar{v}_{34} \cdot \bar{H}_1(\alpha_1 r_i))}{(v_1 v_4 - v_2 v_3)} r' dr' \\
&= \frac{(\bar{v}_{12} \cdot \bar{H}(\alpha_1 r_j^+, \alpha_1 r_i^-)) (\bar{v}_{34} \cdot \bar{H}_1(\alpha_1 r_i))}{\alpha_1^2 (v_1 v_4 - v_2 v_3)} \tag{i}
\end{aligned}$$

$$\begin{aligned}
&\int_{r_j^-}^{r_j^+} \frac{(\bar{v}_{12} \cdot \bar{H}_1(\alpha_1 r_i)) (\bar{v}_{34} \cdot \bar{H}_1(\alpha_1 r'))}{(v_1 v_4 - v_2 v_3)} r' dr' = \\
&= \frac{(\bar{v}_{12} \cdot \bar{H}_1(\alpha_1 r_i)) (\bar{v}_{34} \cdot \bar{H}(\alpha_1 r_j^+, \alpha_1 r_j^-))}{\alpha_1^2 (v_1 v_4 - v_2 v_3)} \tag{iii}
\end{aligned}$$

The vector  $\bar{H}$  is defined by

$$H^{(1)}(z_2, z_1) = \int_{z_1}^{z_2} H_1^{(1)}(\zeta) \zeta d\zeta \quad (B-5)(a)$$

$$H^{(2)}(z_2, z_1) = \int_{z_1}^{z_2} H_1^{(2)}(\zeta) \zeta d\zeta \quad (b)$$

For case (ii) we have for the inner integral

$$\begin{aligned} & \int_{r_j^-}^{r_i} \frac{(\bar{v}_{12} \cdot \bar{H}_1(\alpha_1 r_i)) (\bar{v}_{34} \cdot \bar{H}_1(\alpha_1 r'))}{(v_1 v_4 - v_2 v_3)} r' dr' + \int_{r_i}^{r_j^+} \frac{(\bar{v}_{12} \cdot \bar{H}_1(\alpha_1 r')) (\bar{v}_{34} \cdot \bar{H}_1(\alpha_1 r_i))}{(v_1 v_4 - v_2 v_3)} r' dr' \\ &= \frac{(\bar{v}_{12} \cdot \bar{H}_1(\alpha_1 r_i)) (\bar{v}_{34} \cdot \bar{H}(\alpha_1 r_i, \alpha_1 r_i^-)) + (\bar{v}_{12} \cdot \bar{H}(\alpha_1 r_i^+, \alpha_1 r_i)) (\bar{v}_{34} \cdot \bar{H}_1(\alpha_1 r_i))}{\alpha_1^2 (v_1 v_4 - v_2 v_3)} \quad (ii) \end{aligned}$$

Hence, when these results are substituted into (B-4), we get

$$\begin{aligned} G_{ij} &= j \frac{\sigma_i}{8\pi} \int_{-\infty}^{\infty} e^{-jh(z_i - z_j)} \frac{\sin(h\Delta/2)}{h} (i) dh, \quad r_i < r_j \\ &= j \frac{\sigma_i}{8\pi} \int_{-\infty}^{\infty} e^{-jh(z_i - z_j)} \frac{\sin(h\Delta/2)}{h} (ii) dh, \quad r_i = r_j \\ &= j \frac{\sigma_i}{8\pi} \int_{-\infty}^{\infty} e^{-jh(z_i - z_j)} \frac{\sin(h\Delta/2)}{h} (iii) dh, \quad r_i > r_j, \quad (B-6) \end{aligned}$$

where (i), (ii), (iii) are the corresponding functions presented above for the results of the radial integration, and  $\Delta$  is the width of a cell in the z-direction. We point out that the mesh with which we are working is regular, in the sense that its cells are of constant width in the r- and z-directions.

The expression for  $T_{kj}$  is also easily derived by substituting (A-15)(a) into (23) and interchanging the orders of integration, with the result

$$T_{kj} = \frac{-j\omega\mu_0\sigma_0 n_c}{\pi r_1} \int_0^\infty \frac{\bar{v}_{12} \cdot \bar{H}(\alpha_1 r_i^+, \alpha_1 r_i^-) I(\rho_2 \alpha_0, \rho_1 \alpha_0)}{\alpha_0^2 \alpha_1^2 (v_1 v_4 - v_2 v_3)} \left[ \frac{\cos[h(\zeta_k^- - z_j^-)] - \cos[h(\zeta_k^- - z_j^+)] - \cos[h(\zeta_k^+ - z_j^-)] + \cos[h(\zeta_k^+ - z_j^+)]}{h^2} \right] dh \quad (B-7)$$